

Facile approach to ultra-high single-photon emission purity in an atomically thin semiconductor

Wenjing Wu^{1,2,†}, Alex Strasser^{3,†}, Zhongqi Xiu¹, Hangzheng Shen¹, Song Liu^{4,5}, Luke Nemetz Holtzman⁴, James H. Edgar⁵, James C. Hone⁴, Vasiliy Perebeinos⁶, Junichiro Kono^{1,7,8,9,10}, Xiaofeng Qian^{3,11*}, and Shengxi Huang^{1,7,9,10*}

¹*Department of Electrical and Computer Engineering, Rice University, Houston, TX, USA*

²*Applied Physics Graduate Program, Smalley–Curl Institute, Rice University, Houston, TX, USA*

³*Department of Material Science and Engineering, Texas A&M University, College Station, TX, USA*

⁴*Department of Mechanical Engineering, Columbia University in the City of New York, New York, NY, USA*

⁵*Tim Taylor Department of Chemical Engineering, Kansas State University, Manhattan, KS, USA*

⁶*Department of Electrical Engineering, University at Buffalo, Buffalo, NY, USA*

⁷*Smalley–Curl Institute, Rice University, Houston, TX, USA*

⁸*Department of Physics and Astronomy, Rice University, Houston, TX, USA*

⁹*Department of Material Science and NanoEngineering, Rice University, Houston, TX, USA*

¹⁰*Rice Advanced Materials Institute, Rice University, Houston, TX, USA*

¹¹*Department of Electrical and Computer Engineering, Texas A&M University, College Station, TX, USA*

† These authors contributed equally.

*Corresponding author: Feng@tamu.edu, Shengxi.Huang@rice.edu

Key words: quantum emission, single-photon emission purity, 2D transition metal dichalcogenide, valley polarization, peak-to-background ratio

Single photons, also known as flying qubits, are generated individually, one photon at a time.

Single photons hold enormous potential for driving quantum technologies, such as unhackable communication networks, quantum computers with exponentially higher computational power for particular tasks, and quantum sensors with the sensitivity of single neural cells.

Single photon emission from defect- or strain-engineered 2D transition metal dichalcogenides (TMDs) hold various advantages for future applications of single photons, including the high optical extraction efficiency from the atomically-thin layered materials, zero nuclear spin, and readiness to integrate with on-chip photonic and electronic devices. On the other hand, the quality of single photons generated in 2D TMDs needs considerable improvement to meet application criteria, an important one being single-photon purity. Conventional single photons emitted from 2D TMDs hardly exhibit a purity over 90%, a threshold value key to various applications such as quantum key distribution. In this work, we developed two simple yet effective strategies to enhance single-photon purity in 2D TMDs significantly. In monolayer (ML) WSe₂, we achieved a purity of 98.3% by controlling optical chirality, considering the valley-spin locking of the host material and spin-degenerate defect states. In addition, we used bilayer (BL) WSe₂ and obtained a high purity of 97% even without chirality control, which is due to the inversion symmetry of BL WSe₂. These single-photon purity levels are ultra-high among the reported SPEs from TMDs. Moreover, our methods do not require additional fabrication or instrumentation, and could consistently lead to high-purity single-photon emission. Our work provides deep insights into the electronic, spin, and valley polarizations in 2D TMDs, and present pathways toward generating high-quality single

photons that can be candidate building blocks for future quantum applications.

Solid-state single-photon emitters (SPEs) are desirable for realizing scalable systems and network integration in quantum technologies. For example, atomic defects in solids can form SPEs, with discrete electronic energy levels within the bandgap of the host materials. Archetypal examples include the nitrogen-vacancy (NV) center in diamond¹ and divacancy in SiC². However, in a bulk crystal, the high dielectric constant usually limits the extraction efficiency of SPEs into the external environment to less than 10%, and special design is required to enhance the extraction^{3–5}. Defects at or near the surface will overcome this extraction problem, and provide improved sensitivity, accessibility, and addressability for quantum sensing and control of qubits. 2D host materials naturally possess SPEs at the surface, thus having high photon extraction efficiency. In addition, 2D materials can be readily integrated with on-chip photonic structures such as cavities and waveguides, and SPEs in 2D materials can be tuned via external electric and magnetic fields, as well as through substrate and strain engineering^{6–15}.

Among 2D host materials, transition metal dichalcogenides (TMDs) have become a popular candidate. They possess spin-valley locking allowing for chiral light control with large excitonic binding energies and stable defect-bound states, which make them attractive for SPE host materials^{6,16–22}. SPEs have been discovered in semiconducting TMDs including WSe₂, WS₂, MoS₂, MoSe₂ and MoTe₂.^{18,23–30} SPEs in these materials can be generated through a range of techniques, including strain engineering using patterned substrates like nanopillar arrays and nanoindentation, defect engineering via electron beam irradiation, plasma treatment and chemical doping, allowing

for controllability over emission energy^{27,31–39}. In the most studied material, ML WSe₂, SPEs have demonstrated emissions at energy from 1.52 eV to 1.72 eV, with linewidths typically between 70–800 μeV and lifetimes ranging from 200 ps up to 11 ns. Strain engineering has enabled the tuning of SPE emission energy by up to 200 meV^{16–18,25,26,31,40–46}. Also, SPEs in TMDs can be readily tuned via electric or magnetic fields; for example, tuning of SPE emission energy by 40 meV has been achieved via electric field^{25,42,47–53}. In addition, it has been found that SPEs in WSe₂ can be entangled with phonons^{15,35,49,54–58}. These properties make SPEs in WSe₂ promising for applications in quantum cryptography, on-chip quantum networks, and other photonic quantum information systems like quantum key distribution protocols, such as the emulation of the BB84 protocol⁵⁹.

One crucial metric for evaluating the suitability of SPEs for any quantum application is the purity of emission, which measures the possibility of emitting only a single photon at any given time rather than two or more photons. The second-order auto-correlation function quantifies the purity, $g^{(2)}(0)$, derived from Hanbury Brown and Twiss (HBT) measurement at the specific wavelength. With purity = 1 - $g^{(2)}(0)$, a perfect quantum emitter with $g^{(2)}(0) = 0$ and purity = 100% indicates zero probability of emitting two photons simultaneously and purest single-photon emission. A $g^{(2)}(0)$ value below 0.5 is the criterion of single-photon emission, confirming the quantum nature^{16,18,60–62}. On the other hand, a lower value of $g^{(2)}(0)$ is needed to employ the single photon in various applications. Envisioned quantum circuitry and applications for such emitters typically require $g^{(2)}(0) < 0.01$. For quantum key distribution, achieving $g^{(2)}(0) < 0.1$ is the minimum

requirement. These criteria are seldom met in 2D TMD hosts. Typically, SPEs from 2D TMDs can achieve $g^{(2)}(0)$ values between 0.1 and 0.5^{6,8,16,17,25,61,63–66}. Notably, some works have demonstrated lower $g^{(2)}(0)$ values of less than 0.1. For example, $g^{(2)}(0)$ values of 0.08 and 0.05 have been achieved using strain engineering on van der Waals heterostructures, and lower $g^{(2)}(0)$ values of 0.03 and 0.02 have been demonstrated with graphite contact and atomic force microscopy (AFM) nanoindentation^{35,65–67}.

In TMDs, SPEs typically arise from defect states and strain-induced potentials as shown in Fig 1, but other processes — such as emission from additional defects, exciton complexes, and interband transitions — will significantly impact the single-photon purity and stability^{6,9,15,19,22}. These imperfections give rise to intense, classical light emissions across a broad spectral range, overlapping with the SPE wavelength. Such emissions cannot be effectively filtered out, thereby compromising the purity of single-photon emission to a degree that renders it impractical. Mitigating or eliminating this classical background emission would be an effective approach to enhance the single-photon purity. In particular, methods such as applying electric field via Stark effect, contacting ML TMDs with graphite and molecule, and operating at cryogenic temperatures have been demonstrated to effectively suppress background emissions^{17,68–71}. For instance, researchers have used electrostatic gating to control the emitter's charge environment that can suppress unwanted background emissions and select optical mode in a spin-orbit-coupled microring resonator. This approach has reduced $g^{(2)}(0)$ from 0.13 to 0.031⁷². Also, by integrating ML WSe₂ within a graphite/WSe₂ heterostructure to suppress background, researchers have reduced $g^{(2)}(0)$ from 0.4

to 0.08⁶⁷. Additionally, by creating point-like strain perturbations using pillars with the optimal aspect ratio of 0.3, researchers have achieved $g^{(2)}(0)$ of 0.07 and 0.03 in WSe₂⁷³. On the other hand, these strategies typically require complicated nanofabrication or engineering approaches, and do not lead to high yield of generating high-purity SPEs. Therefore, methods that are simple to implement and effective to consistently generate low $g^{(2)}(0)$ values are necessary to bring TMD SPEs to the next level and meet the requirements of various quantum applications.

Here, we developed two strategies to achieve high purity of single-photon emission from TMDs by suppressing the background from classical emission. In particular, we achieved ultra-high purity of single-photon emissions of 98.3% utilizing optical chirality control on ML WSe₂. While using BL WSe₂, we achieved a high purity of 97.0% even without controlling the optical chirality. In ML WSe₂, due to the valley-spin locking with circular dichroism and the spin-degenerate defect band, we used cross-circular polarization to excite and collect single-photon emission signals, which maintained the intensity of defect emission but largely suppressed the classical background originating mainly from the band-to-band transition. As a result, $g^{(2)}(0)$ for cross-circular polarization achieved an ultra-low value of 0.017, indicating an ultra-high purity of 98.3%. Such an effect is consistently seen in many locations of ML WSe₂. On the other hand, we achieved a high single-photon purity of 97.0% without controlling optical chirality by using BL WSe₂ instead of ML. This is because BL WSe₂ has an indirect bandgap, with spin degeneracy in both valleys and defect bands. Moreover, defect emission from BL maintains a similar transition dipole moment to that of the ML. Thus, the single-photon emission intensity is not compromised while the classical

background is effectively suppressed. Combining ML and BL, from the 59 points we measured, we observed an obvious relation between $g^{(2)}(0)$ and peak-background ratio: a lower $g^{(2)}(0)$ can be achieved with a higher peak-background ratio, confirming our strategy to suppress classical background is valid. Comparing ML and BL WSe₂, we found that BL WSe₂ could easily achieve lower values of $g^{(2)}(0)$ even without controlling the optical chirality, while in ML, $g^{(2)}(0)$ lower than 0.1 were achieved by the cross-circular polarization configuration. Compared to other reports of SPEs from TMDs, our work has achieved ultra-high purity by two simple approaches, polarization control, and BL, without additional fabrication steps or instruments. In addition, our approach led to a relatively high yield of generating high-purity SPEs: among the 59 points we measured, 9 of them achieved single-photon purity over 90%, and 4 of them achieved single-photon purity of 95%. Our findings provided a deeper understanding of the underlying mechanisms governing single-photon emission and paved the way toward the development of high-purity quantum light sources based on 2D materials.

An ML WSe₂ flake exfoliated from high-quality flux-grown bulk crystal⁷⁴ was encapsulated by thin h-BN flakes (thickness < 10 nm) and then transferred on top of predefined dielectric nanopillars using dry transfer technique (see Methods and Fig. S1). The optical microscope image is shown in Fig. 2a, with WSe₂ ML flakes outlined. The grey dots are the nanopillars. Fig. 2b shows the photoluminescence (PL) intensity mapping of the sample at 10 K. It is easy to see that the emission intensity is higher on top of the nanopillars, compared to those off-pillar areas. Ultra-sharp and bright emissions can be seen at cryogenic temperatures. As shown in Fig. S2, at 4 K, multiple

narrow, strong peaks dominate the spectrum between 1.6 eV and 1.7 eV, and the free exciton peak presents at 1.73 eV. With the temperature elevated, intense sharp peaks disappear rapidly, and only the intrinsic exciton peak is observable above 110 K (Fig. S2). At 4 K, well-defined emission features with a full width at half maximum (FWHM) of only a few hundred μ eV are observable at various locations across the sample. The narrow linewidth of these peaks indicates minimal spectral broadening, which is a result of limited exciton diffusion and extended coherence times. These emission peaks, with their narrow spectral bandwidth, are anticipated to exhibit quantum emission characteristics. However, these sharp peaks are superimposed on broad, intense background signals arising from interband transitions and potentially other defects. The energy overlap between these broad background features and the sharp emission peaks poses a challenge, as it compromises the single-photon purity by introducing background photon contamination during experiments (Fig. 1c-e).

The PL spectra of three representative spots, A, B, and C (as labeled in the microscope image Fig. 2a), are chosen to show the significant effect from the spectral background (Fig. 2c-e). We select one sharp peak from each location to discuss the emission characteristics through purity and lifetime analysis. The emitter chosen at spot A is located at 1.682 eV with a FWHM of 0.15 meV (Fig. 2c). The $g^{(2)}(0)$ value is 0.43 ± 0.013 (Fig. 2f), which is less than 0.5 and confirms the single-photon nature^{16,18,61,62}. At spot B, the selected emitter centers at 1.651 eV and has a 0.55 meV FWHM (Fig. 2d). The $g^{(2)}(0)$ value is 0.66 ± 0.051 (Fig. 2g), which indicates this emitter is possibly a hybrid of SPE and classic excitonic emission with the latter taken more proportions⁶⁰.

However, for the peak chosen from spot C, although its FWHM is only 0.75 meV and the intensity is high, which fits the characteristics of most SPEs⁷⁵, its $g^{(2)}(0)$ value is 1.0 ± 0.020 (Fig. 2h). This means that the nature of this peak is dominantly free excitonic emission⁷⁶.

Free excitons have an intrinsically fast decay recombination lifetime in the order of a few tens of ps⁷⁷, owing to their large oscillator strength, which hinders the manipulation of further information transmitted through dissipation or decoherence⁴⁴. The localized exciton has been proven to have a longer lifetime on the order of a few ns^{35,78–80}. According to our results shown in Fig. 2i and j, the lifetime of SPE is longer than that of non-SPE cases. The PL decay curves are fitted with two or three exponential functions, with decay components assigned from short to long as τ_1 , τ_2 and τ_3 . τ_1 and τ_2 are hundreds of ps, while the long decay component τ_3 is longer than 1 ns. For the peak chosen at spot A, the fitted τ_3 in the measured lifetime has a value of 9.9 ± 0.065 ns, those from spots B and C only have values of 5.8 ± 0.050 and 2.9 ± 0.030 , as shown in Fig. 2j. The fitted weight of the long decay τ_3 component for the peak at spot A is 32.2%, much larger than the τ_3 weights for spots B and C (22.4% and 1.1%, respectively), shown in Fig. S3. The SPE at spot A is vulnerable, even with subtle elevation in temperature, $g^{(2)}(0)$ value went up, and the fast decay component became dominant, as shown in Fig. S4.

The experimentally measured radiative decay lifetime (T_1) and FWHM (Γ) are related to each other by $\Gamma = 2\hbar/T_2 = \hbar/T_1 + 2\hbar/T_2^*$ ⁴⁵, where T_2 is the total dephasing time and T_2^* is the pure dephasing time. We fit SPE peaks with a Voigt function, which combines Lorentzian (homoge-

neous) and Gaussian (inhomogeneous) line shapes, allowing us to derive the total dephasing time T_2 specifically from the Lorentzian component. The calculated and measured temporal parameters of sharp peaks from ML are listed in Table S1. We calculated T_2 and compared them with T_1 . The total dephasing time T_2 lay in the range of 5 to 100 ps, which is two orders of magnitude shorter than the radiative decay lifetime T_1 obtained from the experiment (up to 12 ns), indicating our SPEs are in the radiative decay limit⁸¹. Various mechanisms, such as spectral diffusion, environmental perturbations, exciton-phonon interactions, and exciton diffusion, can contribute to the fast dephasing or decoherence.

Although the SPE in Spot A of Fig. 2 exhibits $g^{(2)}(0)$ value of 0.43 that meets the criteria of a single photon, a lower value of $g^{(2)}(0)$ is still needed for practical applications of SPEs. The PL spectra in Fig. 2c-e show a large background; therefore, we need to suppress the background to improve $g^{(2)}(0)$. ML WSe₂ has spin-valley locking due to the strong spin-orbit coupling and broken inversion symmetry, resulting in opposite spin splitting at the K and K' valleys (Fig. 3g). Circularly polarized light selectively excites specific valleys, with bright excitons displaying strong valley circular dichroism^{55,82-84}. To quantify the degree of valley circular dichroism of PL peaks at certain energies, we introduce polarizability $P = (I_{\sigma^+\sigma^+} - I_{\sigma^+\sigma^-})/(I_{\sigma^+\sigma^+} + I_{\sigma^+\sigma^-})$. Here, $\sigma^+\sigma^+$ refers to the experimental configuration of only allowing left-handed circular polarization in both excitation and emission light path, while $\sigma^+\sigma^-$ refers to only right-handed circular polarization signal is allowed in the emission part.

Using different circular polarization configurations in the PL signal excitation and collection, we obtained different spectral intensities at seven different spots (Fig. 3 and Fig. S5). Compared to co-circular polarization for excitation and collection ($\sigma^+\sigma^+$), there is a significant quenching of the broad spectral background using cross-circular polarization configuration ($\sigma^+\sigma^-$). On the other hand, the intensity of the sharp peaks around 1.65 eV remained unchanged when switching between co-circular polarization ($\sigma^+\sigma^+$) and cross-circular polarization ($\sigma^+\sigma^-$). The calculated P values of spectral background and sharp peaks are plotted in Fig. 3c, 3f, and Fig. S5. For the spot shown in Fig. 3a, the broad spectral background has a pronounced P value close to 0.5; in contrast, the P value of the sharp peak located at 1.650 eV is only 0.01. Among all of those spots, spectral background P values are between 0.2 and 0.5, with an average value of 0.71 ± 0.10 , suggesting that the spectral background measured in our sample likely arises from valley-dependent intravalley recombination. P values for most of the sharp emission peaks fall in the range between 0 and 0.2, averaged at 0.05, indicating the absence of valley circular dichroism.

Further, we evaluated the peak-to-background intensity ratio $\alpha = I_{peak}/I_{background}$ for the peaks highlighted in Fig. 3a, d, and Fig. S5. For cross-circular polarization, the highest ratio is 12.23, much larger than the cases for co-circular polarization or non-polarization, which gives the typical ratio smaller than 2 (Fig. S6). The large peak-to-background ratio is indicative to single-photon purity. We assessed the single-photon purity of these sharp peaks across different polarization configurations and found that the cross-circular polarization configuration consistently led to significantly higher peak purity at all seven measurement spots. As shown in Fig. 3b, e, non-polarization

and co-circular polarization configurations yield relatively low purity, with $g^{(2)}(0)$ values of 0.73 and 0.52 (0.66 and 0.60), respectively, suggesting non-single-photon characteristics. On the other hand, under the cross-circular polarization, the $g^{(2)}(0)$ reached exceptionally low values, specifically 0.14 and 0.017, indicating the presence of single-photon emission with extremely high purity. Fig. S5 shows data from five more different spots. Overall, using cross-circular polarization, the measured single-photon purity improved by approximately 50%, achieving an average reduction of $g^{(2)}(0)$ values by a factor of 4.

We also measured the lifetime of the emitters under different optical chirality configurations, as shown in Fig. S7 and Fig. S8. Under cross-circular polarization, where the free exciton contribution is largely filtered out, the temporal decay curve predominantly features a major contribution from radiative decay, with a long lifetime of 5.30 ± 0.08 ns weighted 34.20%. In contrast, under co-circular polarization, the decay curve primarily exhibits the rapid decay characteristic of band-to-band processes (lifetime of 0.34 ± 0.05 ns, weighted 83.12%), suggesting a significant contribution from band-to-band recombination pathways (Fig. S5a). These findings are consistent with the spectra and $g^{(2)}(0)$ measured, indicating a cross-circular polarization configuration can effectively filter out the classical interband transition component. These findings suggest that the purity of single-photon emission can be clearly enhanced by effectively suppressing the spectral background through optical chirality control. Furthermore, the absence of valley circular dichroism in the single-photon emission peaks indicates that the defect states responsible for these emissions in our sample are unlikely to be spin-polarized.

To confirm this, we conducted first-principles calculations of the spin-projected band structures of ML WSe₂ with defects. Given the known significance of Se vacancies in the creation of SPEs in WSe₂⁷⁴, we considered a Se vacancy defect in a 5 × 5 × 1 supercell. The calculated band structure is shown in Fig. 3g. The *K* and *K'* valleys are spin-polarized, meaning they are selective to either the left or right circular polarization of light, which is consistent with the pristine case (Fig. S9). In addition, two pairs of defect bands at 0.67 and 0.86 eV appear as a result of the Se vacancy. Both pairs of defect bands only exhibit very small spin splitting, an effect that diminishes with increasing supercell size, with equal and opposite spin densities (see Fig Sx [in progress]), revealing zero effective spin density. The nearly dispersionless nature of the defect bands is due to the fact that the wavefunction associated with the lower defect bands (Fig. 3h) and upper defect bands (Fig. 3i) are highly localized around V_{Se} . The lack of effective spin density agrees with the absence of valley circular dichroism in the sharp PL peaks from these defect bands, supporting our interpretation that the observed background arises from valley-specific recombination while the SPE peaks are likely attributed to spin-neutral defect states.

As demonstrated above, controlling circular polarization effectively reduces the broad emission background, resulting in a lower $g^{(2)}(0)$ value and higher single-photon purity. However, in some applications, such as sensing chiral molecules or encoding quantum information, light polarization may be needed for purposes other than purity control. This highlights the importance of achieving high single-photon purity independently of light polarization. BL WSe₂ is a promising candidate

platform for this. It has a single-particle bandgap with an indirect nature due to the conduction band energy experiencing a downward shift at the Q point, falling well below that of the K point, and a corresponding upward shift of the valence band edge at the Γ point upon the addition of a second layer (Fig. S10). Its indirect bandgap significantly weakens free excitonic emission compared to ML. Naturally, BL has $2H$ stacking with the top layer 180 degrees rotated with regard to the bottom layer. The preservation of inversion symmetry results in a lack of valley circular dichroism. In addition, it can still host SPEs with transition dipole moments comparable to those from ML^{49,85}. Therefore, we examined the capability of generating single photons from BL WSe₂ and the corresponding purity.

The SPEs hosted by BL have emission energy between 1.5 and 1.6 eV, approximately 0.1 eV lower than those from ML (Fig. 4a and Fig. S11). This spectral range aligns well with the requirements for quantum memory applications^{86,87}. The linewidth of the SPE peaks from BL is from 0.14 to 0.71 meV. The peak-to-background intensity ratio α values lay between 10 and 23 under both optical chirality, as shown in Fig. S12. The lifetime of the selected SPE peak in Fig. 4a is 12.05 ± 0.01 ns, longer than the longest SPE lifetime from the ML mentioned above (Fig. 4c). In addition, this radiative decay curve can be fitted with a single exponential function, indicating that there is only one single-photon emission process dominating the decay. The $g^{(2)}(0)$ value of this peak is as low as 0.030 ± 0.0030 without polarization selection, shown in Fig. 4b.

Circular polarization control was also applied to the BL samples to confirm the absence of valley

circular dichroism. Comparing co- and cross-circular polarizations, we found minimal changes in both SPE peak and spectral background intensities, as presented in Fig. 4d and Fig. S13. The average P values of SPE peak and background in Fig. 4d were 0.02 and 0.01, respectively, with the difference as small as 0.01. Additionally, no significant variations in purity values $g^{(2)}(0)$ were observed across different polarization configurations; for the upper (lower) panel of Fig. 4e, $g^{(2)}(0)$ for cross-circular and co-circular polarizations are 0.093 (0.178), and 0.098 (0.201), respectively, very close to each other. All of these experimental results support the hypothesis that the BL can host high-purity single-photon emission independently of light polarization.

Our first-principles calculations further confirmed that both intrinsic and defected emissions from BL WSe₂ lack valley spin polarization. As illustrated in Fig. 4h, the defect bands that arise at 0.66 eV and 0.83 eV are flat, doubly degenerate, and exhibit zero effective spin polarization. Although individual layers of pristine BL WSe₂ have spin splitting at the K and K' valleys similar to the ML case, the presence of both inversion symmetry and time-reversal symmetry in pristine BL WSe₂ guarantees doubly degenerate states with opposite spin throughout the entire Brillouin zone, resulting in effective zero spin polarization in total, as shown in Fig. S10. The presence of a V_{Se} defect leads to mild inversion symmetry breaking and thus a small spin splitting in the case of 5 × 5 × 1 supercell, although the bands become more degenerate with increasing supercell size. The resulting spin densities are equal in magnitude with opposite sign in the nearly degenerate highest valence bands (Fig. 4i) and lower defect states (Fig. 4j), ensuring zero effective spin density. This theoretical result further validates that SPEs from BL WSe₂ have no spin valley selection, high-

lighting their potential for polarization-sensitive quantum applications.

To understand the observation that the SPE intensities in BL are comparable to that in ML, we calculated optical excitation intensities from the defect states. Due to the large supercell with spin-orbit coupling taken into account, the frequency-dependent optical absorption coefficient was calculated using first-principles DFT in the independent particle approximation, as shown in Fig. S14 and Fig. S15. The Se vacancy induced excitation intensity was obtained by the integration over the energy range for the associated defect states, which shows comparable total intensities from ML and BL WSe₂ (1.15×10^{-4} eV for ML and 1.23×10^{-4} eV for BL). Indeed, the defect states largely reside in the W's *d* orbitals and Se's *p* orbitals in both ML and BL WSe₂, while the bilayer structure does not have a significant impact on the electronic wavefunctions associated with the defects and the nearby bulk states. Thus the transition intensity should be similar.

We measured a total of 59 $g^{(2)}(0)$ values at 48 different locations, including ML and BL, and 9 of them were examined with chirality control. We summarize the $g^{(2)}(0)$ values statistically in Fig.5. Fig.5a summarizes the relation between the peak-to-background ratio and $g^{(2)}(0)$. The peak-to-background ratio α can effectively quantify the weight of emissions at the same energy from a quantum emission nature compared to classic excitonic ones. From Fig. 5a, it is clear that with larger α , $g^{(2)}(0)$ value is generally smaller. For high purity emitters with $g^{(2)}(0) \leq 0.1$ that meet the quantum key distribution requirement, α needs to be larger than 5.

When comparing the BL to the ML, we calculated the mean $g^{(2)}(0)$ values to be 0.28 ± 0.08 and 0.54 ± 0.09 for BL and ML, respectively. (Fig 5b) Therefore, BL generally exhibits lower $g^{(2)}(0)$ values, meaning that it tends to produce reliable single-photon emissions with higher purity. Among the 25 $g^{(2)}(0)$ values measured in BL and 34 measurements in ML, the BL showed 9 (5) spots with $g^{(2)}(0)$ values lower than 0.2 (0.1), while the ML had only 5 (4) such spots. In addition, these lower values in ML were all achieved with spectral background suppressing by cross-circular polarization configuration. In contrast, for the $g^{(2)}(0)$ values lower than 0.2 (0.1) in BL, most of them were achieved with unpolarized light. We summarized the reported SPEs in WSe₂ with relatively low $g^{(2)}(0)$ values in Table 1. Compared to other works, our study achieved ultralow $g^{(2)}(0)$ and ultrahigh purity: $g^{(2)}(0)$ is 0.017 from chirality controlled ML and 0.030 from BL, corresponding to the purity of 98.3% and 97.0%, respectively. It is worth noting that although several other works also achieved low $g^{(2)}(0)$ ^{6,8,16,17,25,35,61,63–65,65–67,88}, our approaches, chirality control and BL TMD, can consistently yield low $g^{(2)}(0)$ (14 spots with $g^{(2)}(0) < 0.2$ out of 59 spots), without additional nanofabrication steps or instruments.

In conclusion, we developed two effective approaches to approach the intrinsic purity of the SPEs from atomically thin WSe₂. We have demonstrated significant suppression of background emissions in ML WSe₂ with cross-circular polarization of optical excitation and detection, suggesting that the broad background emissions from 1.6 eV to 1.7 eV likely originate from intra-valley recombination processes. Notably, despite the chirality control, the absolute intensity of the SPE peak remains consistently robust. This observation underscores the stability and reliability of SPE emission under different experimental conditions. Our results highlight the efficacy of cross-

Table 1: Summary of SPE purity in WSe₂

Sample	Strain and defects	$g^{(2)}(0)$	Refs
ML	As exfoliated	0.18 ± 0.020	Ref ¹⁶
ML	Nanopillar	0.087 ± 0.065	Ref ⁶⁵
ML	Nanopillar, E-beam irradiation	0.05 ± 0.040	Ref ³⁵
BL	As exfoliated	0.20	Ref ⁸⁵
Thick flake	As exfoliated	0.25	Ref ¹⁸
ML	AFM tip indented	0.070 ± 0.010	Ref ⁷⁸
ML	AFM tip indented	0.020	Ref ³⁶
ML	Nanopillar	0.017 ± 0.0072	Our work
BL	Nanopillar	0.030 ± 0.0030	Our work

circular polarization detection for SPEs in ML WSe₂, consistently yielding $g^{(2)}(0)$ values below 0.1. Moreover, our findings indicate that BL is a superior host material due to its momentum-dark excitonic nature, resulting in a lower spectral background than ML. Additionally, BL exhibits minimal valley polarization, enabling high-purity single-photon emission without polarization selection. This accomplishment represents a significant advancement in enhancing the purity and fidelity of SPE emission measurements, which is crucial for various applications such as quantum information processing and secure communication protocols. Overall, our findings contribute to a deeper understanding of the photophysical properties of SPEs in 2D materials.

Methods

Sample fabrication and characterization WSe₂ ML and BL were mechanically exfoliated from flux-grown bulk crystals. Individual flakes were identified under the optical microscope by color contrast and then confirmed by the E_{2g} phonon frequency using Raman spectroscopy. Thin hBN flakes were exfoliated from boron isotope-pure crystals. The encapsulated WSe₂ ML and BL samples were fabricated using the stamp dry transfer method. A thin polypropylene carbonate (PPC) polymer film was used to pick up the top hBN flake. This hBN was used to pick up all the rest of the 2D flakes one by one. The whole stack was released on pre-fabricated nanopillars by melting the PPC film, then the polymer residue was washed away by acetone.

285 nm SiO₂/Si substrate was used to fabricate nanopillar arrays. Individual pillar has a diameter of 200 nm and a height of 100nm; the separation between pillars is 2.5 μ m. The array was patterned by electron beam lithography (Elionix ELS-G100) with PMMA 950 A3 resist. A layer of 50 nm Cr was evaporated after developing, and after liftoff, the SiO₂ was etched 100 nm by reactive ion

etching (Oxford Plasmalab). The Cr hard mask was etched away by Cr etchant (Sigma-Aldrich). The nanopillar array structure was imaged and confirmed by the scanning electron microscope (FEI Apreo).

Optical spectroscopy measurements

Steady-state PL measurements

The PL measurements were performed on the Renishaw InVia confocal microscope system, with the optical path connected to a liquid-helium recirculating optical cryostat (Montana Instruments CryoAdvance50 with Cryo-Optic module). A vacuum-compatible 100X, NA 0.90 objective (Zeiss LD EC Epiplan-Neofluar 100x/0.90 DIC M27) was mounted inside the cryostat. In all measurements in this study, the samples were at 4 K in vacuum, otherwise stated. A CW laser centered at 532 nm with a maximum output power of 52 mW was used as excitation. The incident laser power was controlled below 100 nW in all measurements to eliminate local heating. All the PL spectra are reproducible in repeated measurements at the same spot on the sample.

Time-correlated single photon counting (TCSPC) measurements

All TCSPC measurements were performed based on the MicroTime100 microscope (PicoQuant) coupled with the TimeHarp 260 time-counting module(PicoQuant), with an optical path to Montana Instrument CryoAdvance50 with a Cryo-Optic module, the same as the steady-state spectroscopy measurements. 509 nm 40 MHz pulse laser (PicoQuant LDH-D-C-520) was used to

excite the sample, with laser power below 50 nW to avoid heating. The emission signal was selected by hard-coated bandpass filters center at specific peak energies (Thorlabs, FWHM = 10 nm), then collected by single-photon avalanche photodiodes(SPAD) (Excelitas SPCM-AQRH-14-TR).

Single-photon purity measurement and fitting

Second-order autocorrelation measurements were performed using an HBT interferometer setup consisting of one 50:50 beamsplitter and two SPADs. The emission signal was selected by two hard-coated bandpass filters before two SPADs and then correlated with a TimeHarp 260 time-counting module. The $g^{(2)}(\tau)$ data measured and reported in this work are without background correction. The curves were fitted with a single exponential function. An n -peak fitting function is defined below:

$$D(t) = \sum_{n=0}^N \left(a + b_n \cdot \exp\left(-\left|\frac{t - t_n}{\tau_n}\right|\right) \right)$$

where n represents the peak number, a is a constant baseline parameter, b_n is the peak height factor, t_n denotes the peak center position, and τ_n is the corresponding decay lifetime. By computing the standard deviation of the peak height and the baseline, we observed that the minor random fluctuations in peak height were attributable to the system response, with a bin width of 100 ns for the data presented. We set each peak's height factor b_n to their respective maximum values to ensure better overlap and achieve a more precise peak area calculation. After determining the values of a , b_n , t_n , and τ_n , the area of the n -th peak was calculated through integration over the interval $[t_n - 15, t_n + 15]$. This approach allowed us to account for the specific characteristics of each peak and ensured accurate area measurements. The integral used for this calculation is

expressed as follows:

$$A_n = \int_{t_n-15}^{t_n+15} \left(a + b_n \cdot \exp\left(-\left|\frac{t-t_n}{\tau_n}\right|\right) \right) dt$$

The value of $g^{(2)}(0)$ is defined as the ratio $\frac{A_0}{A_{\text{adj}}}$, where A_0 is the area under the curve of the peak at zero delay time, and A_{adj} is the area under the curve of the peak adjacent to it. For the sake of precision, the value of A_{adj} is determined by averaging the area values of 8 adjacent pulse peaks. This method ensures a more reliable and accurate measurement by minimizing the impact of any potential anomalies or variations in individual peak areas.

Theoretical calculation

Atomic structure optimization of monolayer and bilayer WSe₂

First-principles calculations were carried out by using density functional theory (DFT)^{89,90} as implemented in the Vienna Ab initio Simulation Package (VASP)^{91,92} with the projector augmented wave (PAW) method⁹³ to efficiently treat the core electrons, the Perdew-Burke-Ernzerhof form⁹⁴ of exchange-correlation energy functional in the generalized gradient approximation, the Grimme's DFT-D3 method⁹⁵ with zero-damping function to properly take into account the weak interlayer dispersion interactions, and the plane-wave basis with an energy cutoff of 400 and 250 eV for structural optimization of pristine unit cell and large $5 \times 5 \times 1$ supercell with Se vacancy defect, respectively. The Monkhorst-Pack k-point sampling method⁹⁶ was applied for Brillouin zone integration, with a $10 \times 10 \times 1$ grid for the optimization of the pristine unit cell without defect and a $2 \times 2 \times 1$ grid for the optimization of the supercell with Se vacancy. A vacuum layer of 15 Å was added to minimize the artificial image interaction between 2D materials due to the

periodic boundary condition applied in the DFT calculations. All the structures were fully relaxed with the maximum residual force of less than 0.01 eV/Å and the convergence criteria for electronic relaxation of less than 10^{-6} eV.

Electronic structures of Se vacancy in monolayer and bilayer WSe₂

In the dilute limit the electronic states associated with the Se vacancy defect should be fully localized without strong dispersion in the electronic band structure. Therefore, to mimic the dilute limit while balancing the computational cost, a large supercell of $5 \times 5 \times 1$ was adopted to minimize the periodic image interaction of Se vacancy along the in-plane directions and a plane-wave basis with an energy cutoff of 200 eV was used for both self-consistent calculation and band structure calculation. Spin-orbit coupling was taken into account to capture the valley spin splitting in WSe₂. As the large supercell size and the reduced symmetry with spin-orbit coupling make it computationally challenging to solve two-particle Bethe-Salpether equation in monolayer and bilayer WSe₂, the electronic structure calculations were performed at the DFT level. Furthermore, charge density $\rho_{n\mathbf{k}}^I(\mathbf{r})$ and spin densities $\{\rho_{n\mathbf{k}}^x(\mathbf{r}), \rho_{n\mathbf{k}}^y(\mathbf{r}), \rho_{n\mathbf{k}}^z(\mathbf{r})\}$ of the Se vacancy derived electronic states were calculated by first extracting the Kohn-Sham eigenfunctions $|\psi_{n\mathbf{k},\alpha}\rangle$ associated with the defect and then calculating the spatially-resolved expectation values, $\rho_{n\mathbf{k}}^i(\mathbf{r}) \equiv \sum_{\alpha,\beta} \psi_{n\mathbf{k},\alpha}^*(\mathbf{r}) \sigma_{\alpha\beta}^i \psi_{n\mathbf{k},\beta}(\mathbf{r})$ with $i = \{I, x, y, z\}$, where σ^I is a 2×2 identity matrix and $\{\sigma^x, \sigma^y, \sigma^z\}$ are three 2×2 Pauli matrices. n denotes the band index, \mathbf{k} denotes the wave vector, and $\{\alpha, \beta\}$ denote the spinor component of the wavefunctions.

Band unfolding in monolayer and bilayer WSe₂ with and without Se vacancy

Due to the $5 \times 5 \times 1$ supercell used in the electronic structure calculation of the Se vacancy defect, the electronic band structure is a mix of defect states and the electronic states from pristine ML and BL WSe₂. As a result, electronic bands are folded into the small first Brillouin zone of the supercell. In order to compare with the pristine band structure, we perform a band unfolding analysis ^{97,98}, shown in Fig. Sxx. From the comparison between the unfolded supercell band structure and the pristine band structure, we see that the majority of the unfolded bands from the supercell come directly from the pristine unit cell. The thickness of the dispersed unfolded bands are based on their spectral weighting, corresponding to how the unfolded bands align in the first Brillouin zone of pristine unit cell. The absence of spectral weight near the defect bands is due to the localization of the defect states. The defect states do not have additional weight from the unfolded bands. The spectral weight of BL WSe₂ across the non-defect bands is higher than that in ML WSe₂, corresponding to their doubly degenerate states of bilayer under the inversion symmetry except the defect.

Theoretical comparison of SPE intensity in monolayer and bilayer WSe₂ with Se vacancy

Due to the large supercell and reduced symmetry with spin-orbit coupling taken into account, we approximate the SPE intensity by calculating the total optical excitation intensity at the DFT level under the independent particle approximation. Specifically, we first calculate the frequency-dependent optical absorption coefficient $\alpha(\omega)$, shown in Fig. S14 and Fig. S15. Based on the Beer-Lambert Law, the optical excitation intensity over a range of frequencies from ω_1 to ω_2 is

given by $I_{\text{abs}} = \int_{\omega_1}^{\omega_2} [1 - e^{-\alpha(\omega)L}] d\omega$. The thicknesses (L) used were based on the crystal structure with a 3.4 Å van der Waals radius, which were 7.0 Å for monolayer and 13.4 Å for bilayer. Integrating across the frequency range of the defect states reveals comparable total optical excitation intensities, supporting comparable SPE intensities in ML and BL WSe₂. The integral was first performed over the smallest primary defect peak, from 0.89 to 0.96 eV, with a result of 1.40×10^{-5} eV for monolayer and 1.25×10^{-5} eV for bilayer. The integral was also performed over all the defect band absorption peaks, from 0.89 to 1.25 eV, with a result of 1.15×10^{-4} eV for monolayer and 1.23×10^{-4} eV for bilayer. The energy range is not the same as the SPE because DFT underestimates the value of the bandgap. The comparable integrated intensities support comparable SPE intensities in ML and BL WSe₂.

Acknowledgment

WW and SH acknowledge the support from the National Science Foundation (Grant No. ECCS-2246564), the Air Force Office of Scientific Research (AFOSR, Grant No. FA9550-22-1-0408), and the Robert A. Welch Foundation (Grant No. C-2144). JK acknowledges support from the Robert A. Welch Foundation (Grant No. C-1509). AS and XQ acknowledge the support from the National Science Foundation under Grant No. DMR-2103842 and DMR-1753054, as well as the advanced computing resources provided by Texas A&M High Performance Research Computing.

Author Contribution

WW and SH conceived the idea. WW fabricated the samples and performed the measurements under the supervision of SH and JK. WW analyzed the data with the help of ZX and HS. AS, XQ,

and VP performed the theoretical calculations and analyses. SL and JHE provided hBN crystal. SL, LNH, and JH provided WSe₂ bulk crystal. All authors participated in the discussion and wrote the manuscript.

Figures

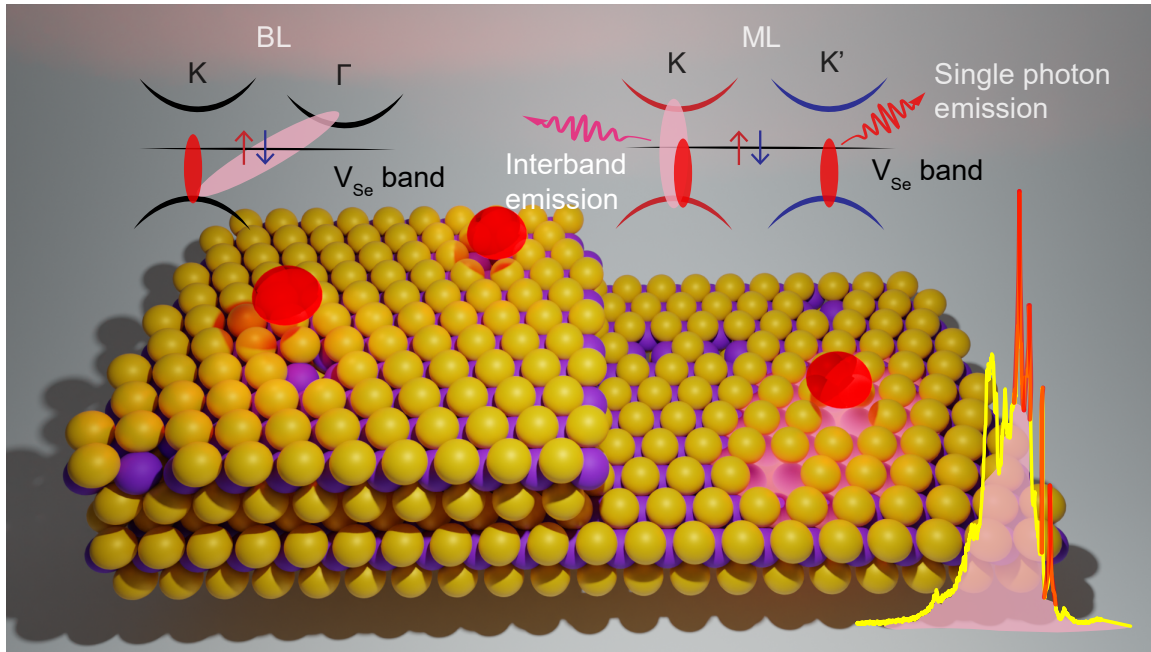


Figure 1: Illustration of the strain-engineered WSe₂ SPEs. Schematic of strained WSe₂ ML encapsulated between top and bottom hBN on nanopillar substrate.

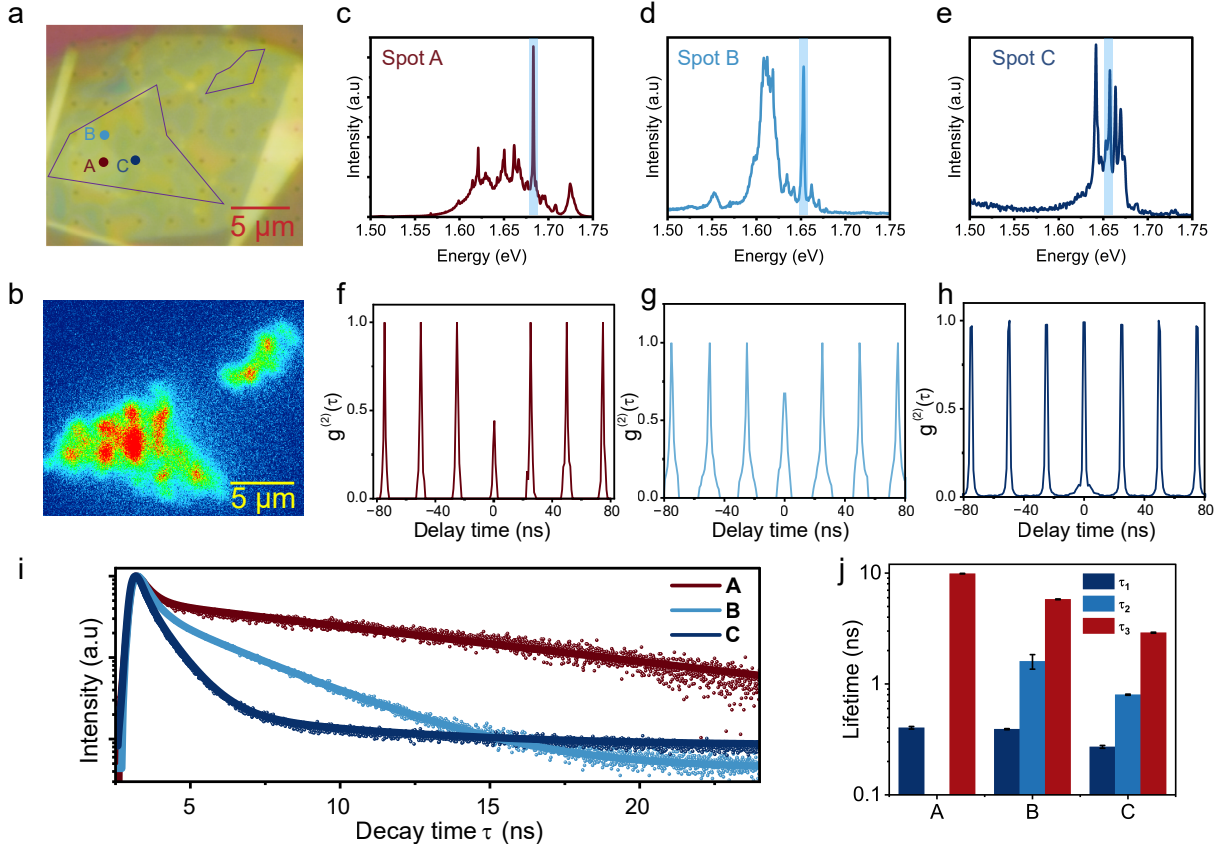


Figure 2: Measured single-photon purity affected by the broad spectral background under the sharp emissions. **a.** Optical microscope image of the hBN/ML WSe₂/hBN sample on top of nanopillars. ML WSe₂ regions are outlined. Spots A-C in **c-e.** are denoted with matched colors. **b.** PL intensity mapping of the sample at 10 K. **c-e.** PL spectra of spots A-C, selected peaks for photon statistics, and time-correlated analysis are highlighted with a light blue box. **f-h.** Measured second-order correlation functions $g^{(2)}(\tau)$ curves of selected peaks in **c-e**, respectively; The fitted $g^{(2)}(0)$ values are 0.43 ± 0.013 , 0.66 ± 0.051 , 1.0 ± 0.020 . **i.** PL decay curves of the selected peaks. **j.** Fitted lifetime components from the decay curves.

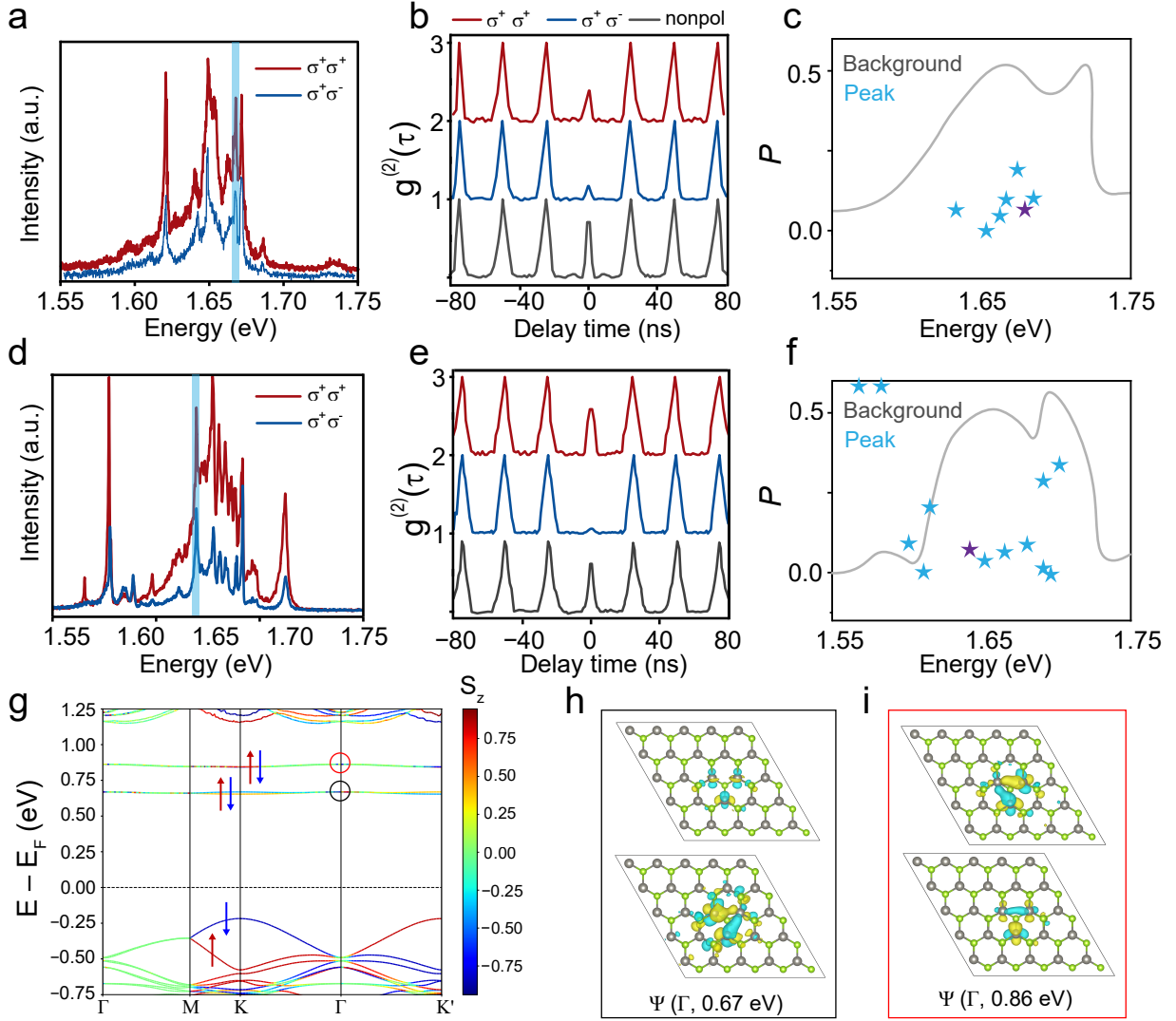


Figure 3: Improving the purity of single-photon emission by polarization selection. **a[d].** PL spectra measured with $\sigma^+\sigma^+$ (dark red) and $\sigma^+\sigma^-$ (navy) configurations at two different spots. **b[e].** Second-order correlation function $g^{(2)}(\tau)$ curves measured with $\sigma^+\sigma^+$ (blue), $\sigma^+\sigma^-$ (red), and non-polarization (gray) configuration. Selected peaks are highlighted with a light blue box in **a[d]**. **c[f].** Calculated P values of spectral background (grey lines) and peaks (light blue stars) at different energy for **a[d]**, the purple stars represent the selected SPE peaks. **g.** Spin S_z projected band structure of ML WSe₂ with V_{Se} defect in a $5 \times 5 \times 1$ supercell from first-principles calculation. **h[i]** Real component of the α spinor at the Γ point for the lower defect state **[h]** and upper defect state **[i]**.

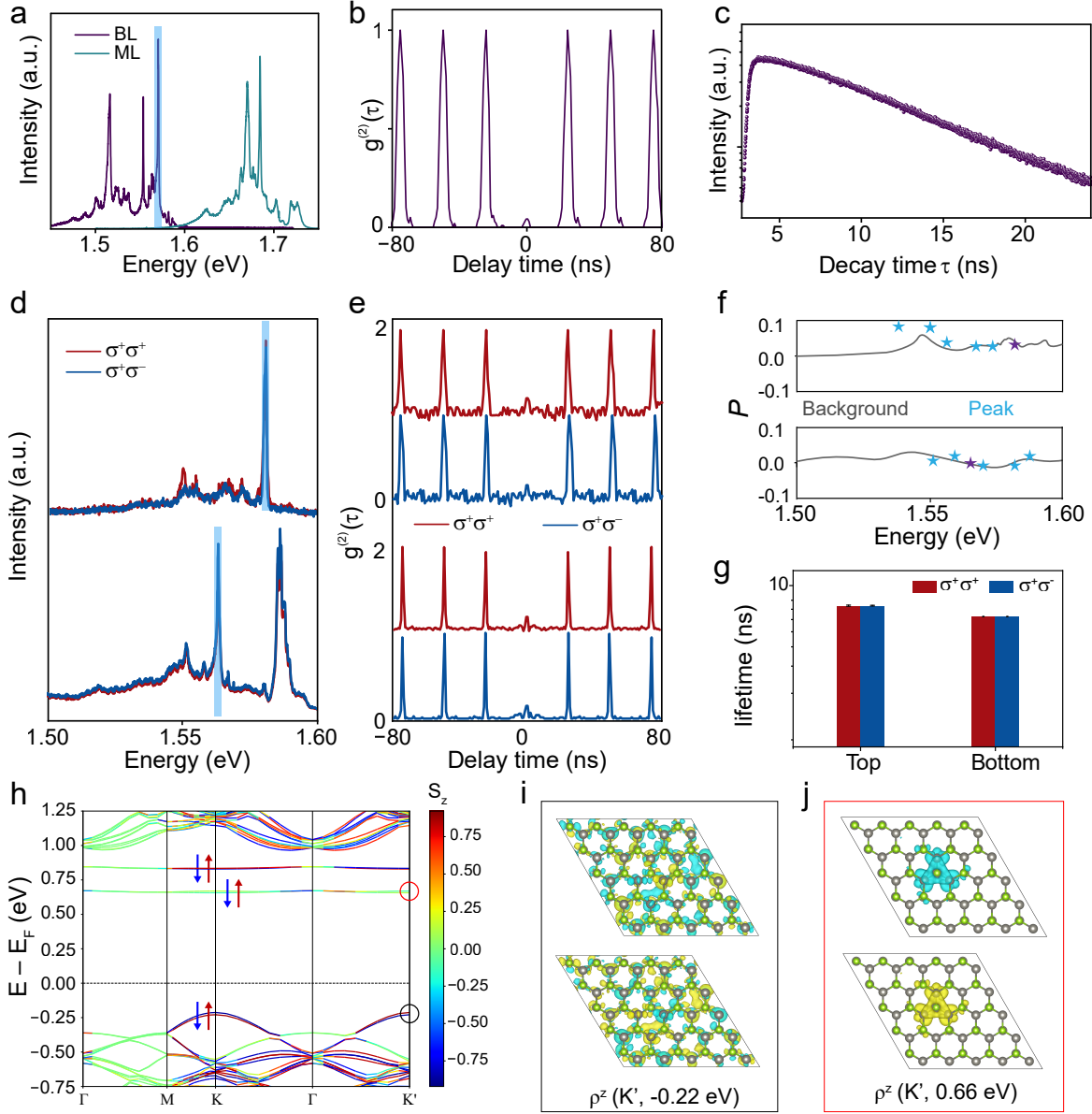


Figure 4: High purity of single-photon emission in BL WSe₂. **a.** Comparison of PL spectra of strained ML (cyan) and BL (purple) WSe₂. **b.** $g^{(2)}(\tau)$ curve of the selected peak, $g^{(2)}(0) = 0.030 \pm 0.03$. **c.** PL decay curve of the highlighted peak in **a**, lifetime $\tau = 12.05 \pm 0.09 \text{ ns}$. **d.** PL spectra with different optical chirality at two different spots. **e.** $g^{(2)}(\tau)$ curves measured with $\sigma^+\sigma^+$ (blue) and $\sigma^+\sigma^-$ (red) polarization for the peaks highlighted in **d**. The fitted $g^{(2)}(0)$ values are 0.093 ± 0.010 , 0.098 ± 0.011 , 0.178 ± 0.040 , and 0.201 ± 0.082 , from top to bottom. **f.** P values of spectral background (grey lines) and peaks (light blue stars) at different energy for **d**, the purple stars represent the selected SPE peaks. **g.** Measured the lifetime of selected peaks in **d** top and bottom panels with different polarization configurations. **h.** Spin S_z projected band structure of BL WSe₂ with V_{Se} defect in a $5 \times 5 \times 1$ supercell from first-principles calculation. **i[j]** Spin density S_z at K' of the highest valence bands [**i**] and lower defect states [**j**].

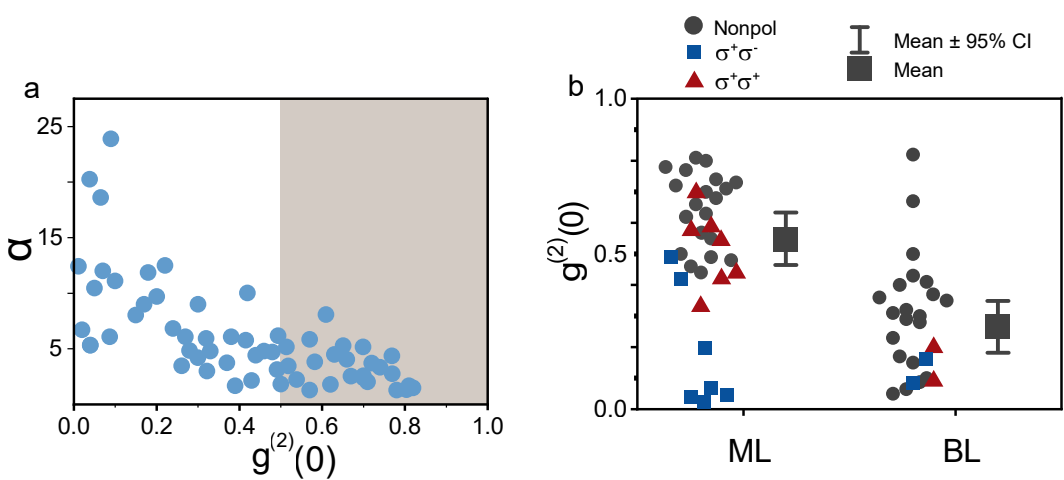


Figure 5: Summary of peak-to-background α and $g^{(2)}(0)$ values of all peaks analyzed in ML and BL WSe₂. a. Calculated α values with regard to the $g^{(2)}(0)$ of the peaks. **b.** All $g^{(2)}(0)$ values of peaks in ML and BL with different polarization configurations. (Red triangle: co-polarized, blue rectangle: cross-polarized, gray dots: non-polarized)

Supporting Information

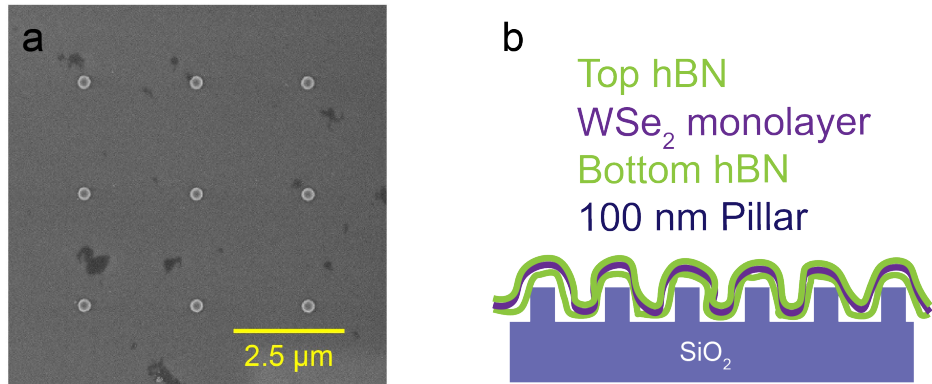


Figure. S1: Strain engineered substrate and sample geometry. **a** Scanning electron microscopy image of the nanopillar on the substrate. **b** Schematic of sample geometry, WSe₂ monolayer is sandwiched by top and bottom hBN (both ≈ 10 nm thick) .

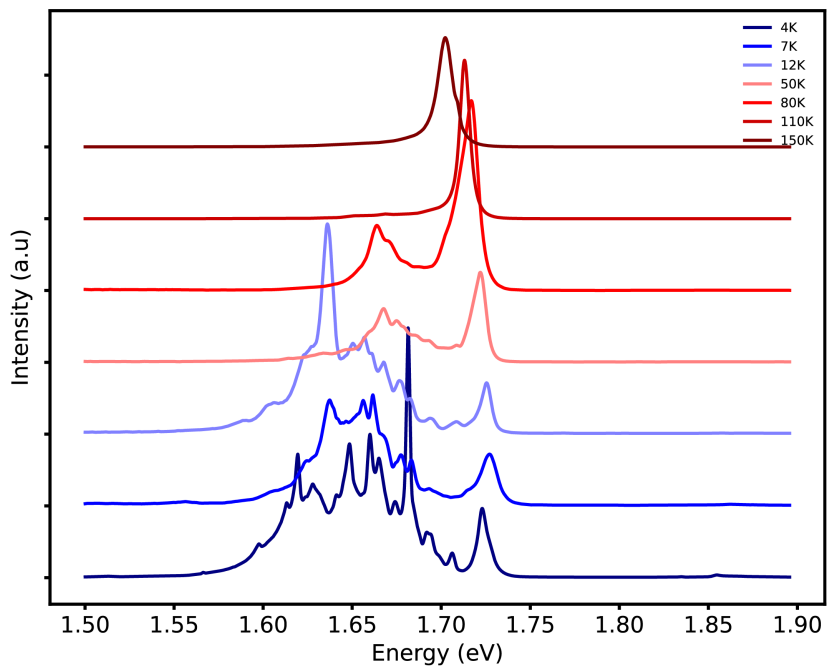


Figure. S2: Temperature dependent PL spectra of strained WSe₂ monolayer.

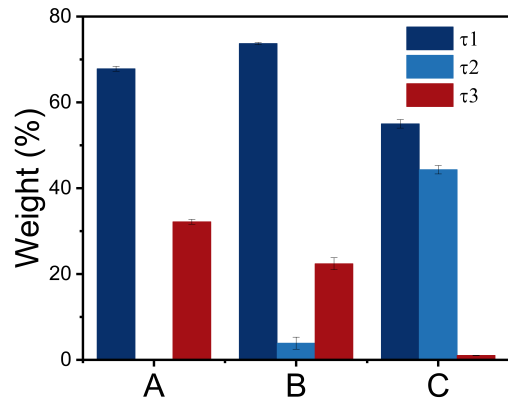


Figure. S3: Different decay component weight calculated for the lifetime of selected peaks at spot A, B, C.

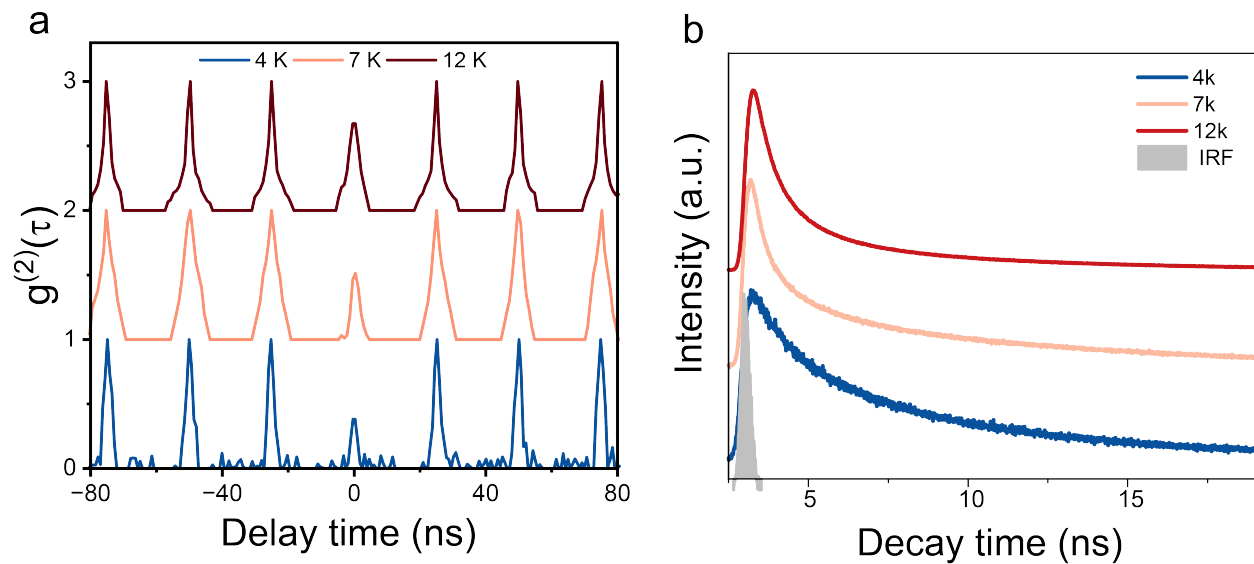


Figure. S4: Temperature dependence of $g^2(\tau)$ and PL decay curve of the peak selected in Fig. 2c at spot A.

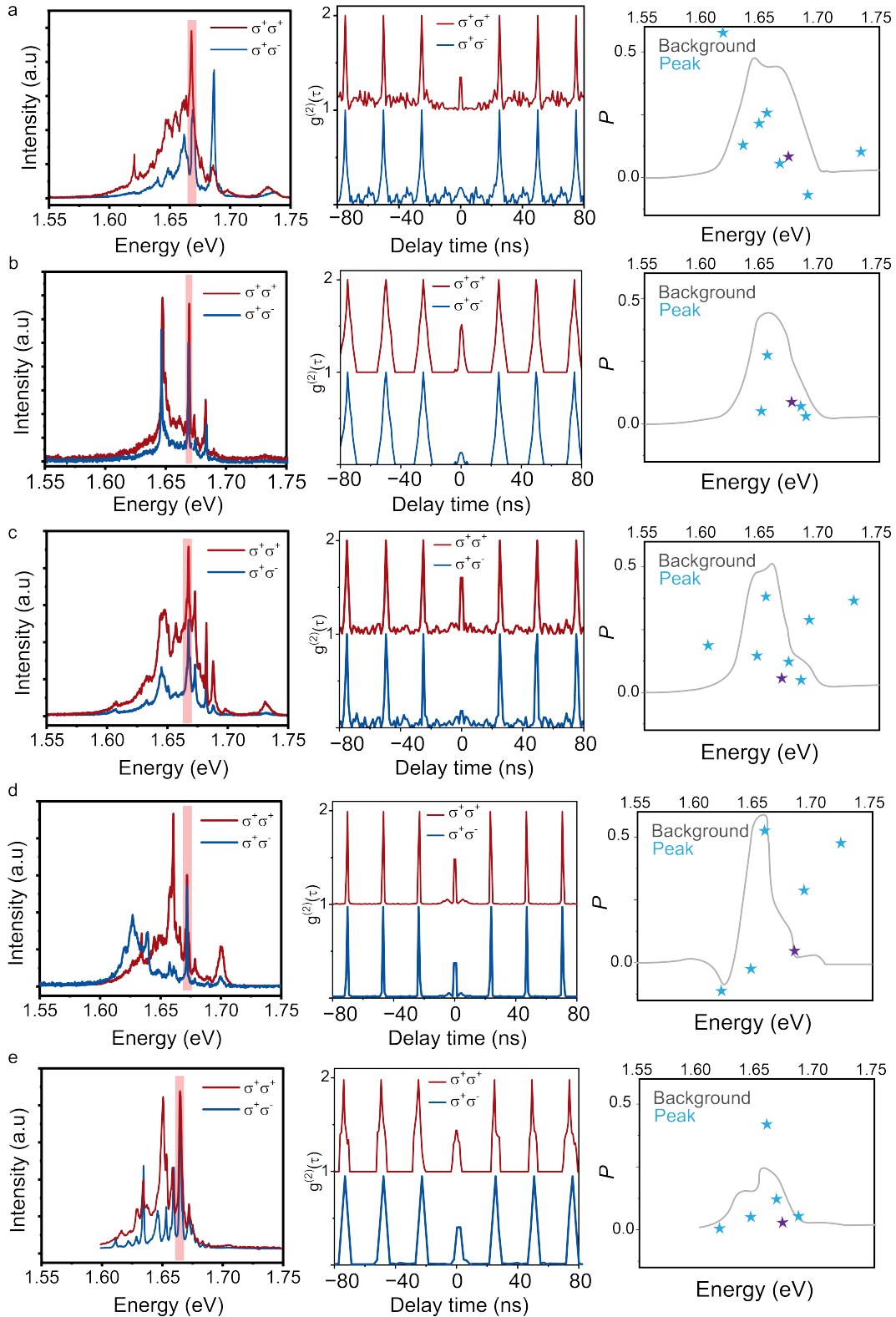


Figure. S5: Five extra spots on ML with SPE peak characteristic analysis.

Table. S1: Lifetime calculated from peak linewidth and experiment results of spots in monolayer and bilayer WSe₂

Spot	FWHM (meV)	Total dephasing time T ₂ (ns)	Lifetime T ₁ (ns)
Monolayer Spot 1	0.71	0.018	9.9
Monolayer Spot 2	0.68	0.020	2.1
Monolayer Spot 3	2.00	0.007	1.7
Monolayer Spot 4	1.08	0.012	5.3
Bilayer Spot 1	0.70	0.019	6.5
Bilayer Spot 2	0.14	0.094	12
Bilayer Spot 3	0.39	0.034	7.6
Bilayer Spot 4	0.71	0.018	6.1

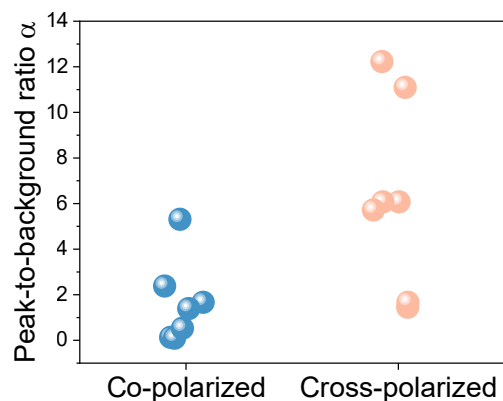


Figure. S6: Peak-to-background ratio α of SPEs in ML using different polarization configurations.

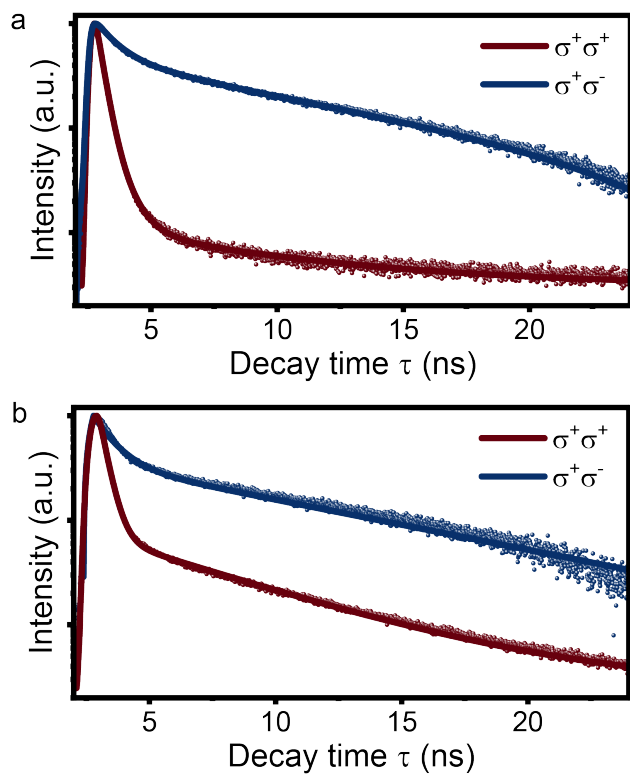


Figure. S7: PL decay curves of the peak selected in Fig. 3a and d with different polarization configurations

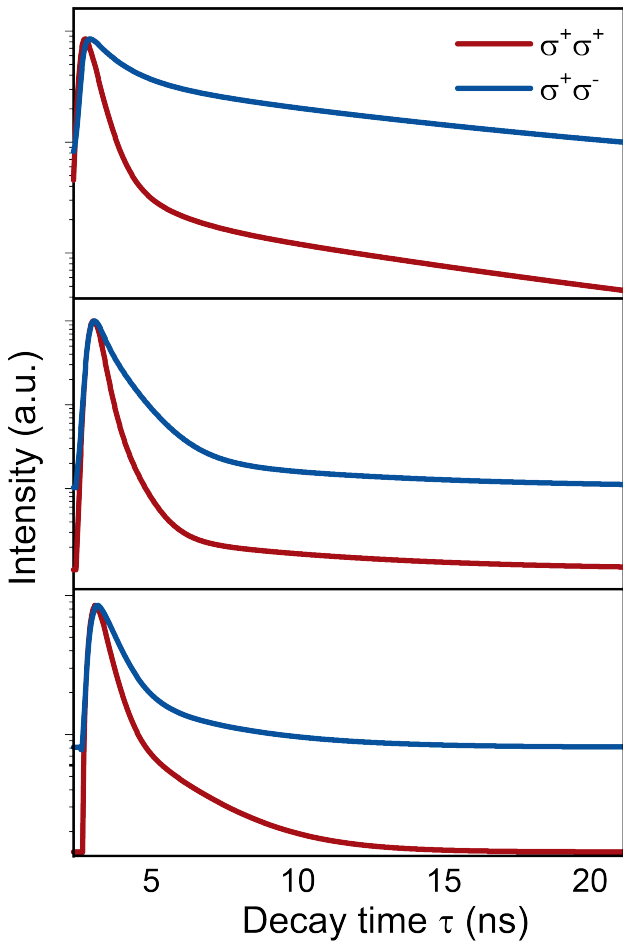


Figure. S8: PL decay curves of the peak selected in Fig. S5a-c with different polarization configurations.

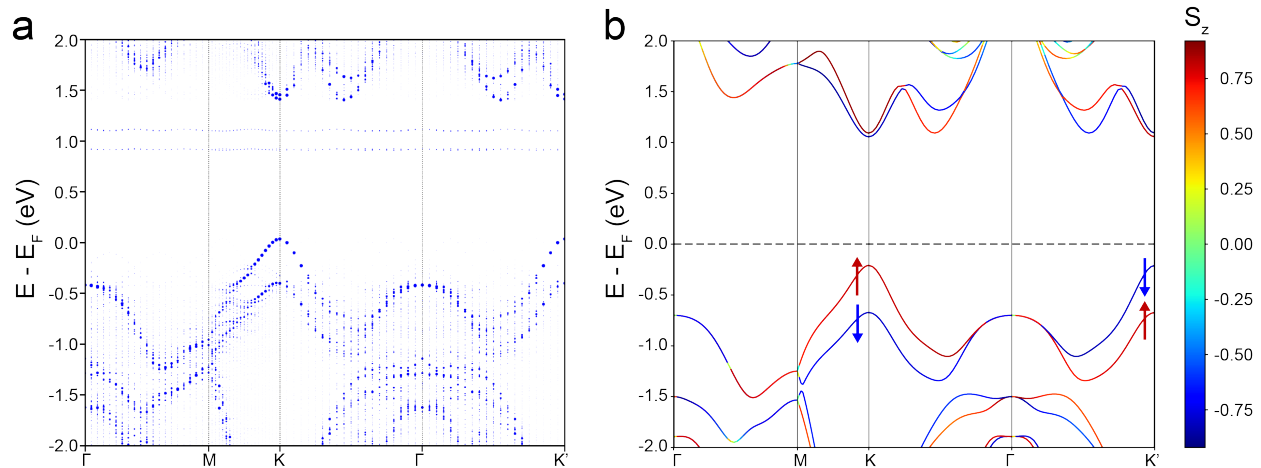


Figure. S9: Band structure of pristine monolayer WSe₂ from first principles calculation.

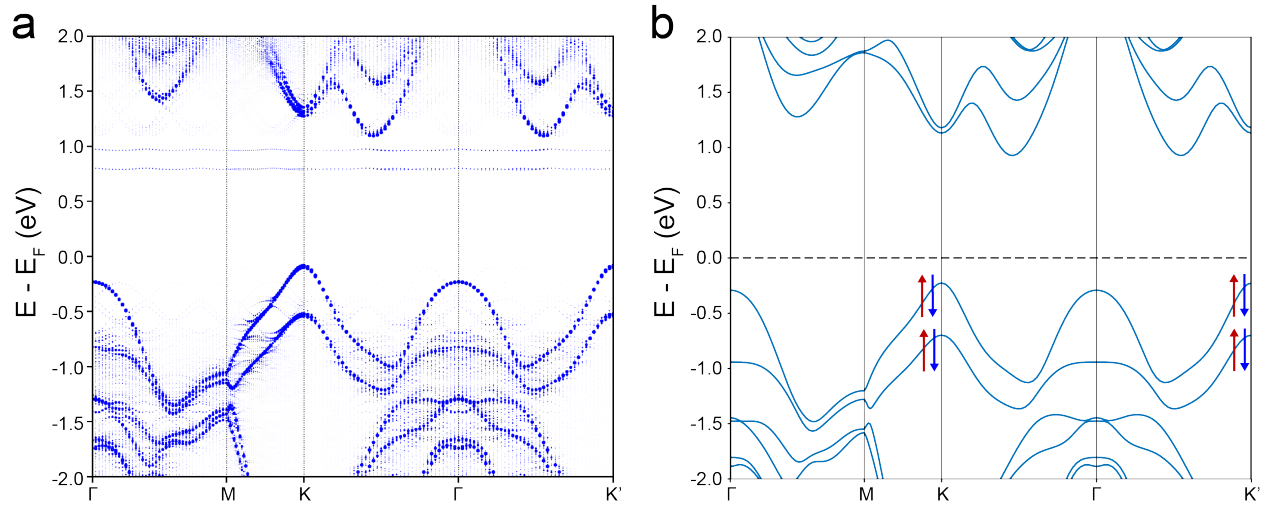


Figure. S10: Band structure of pristine bilayer WSe₂ from first principles calculation.

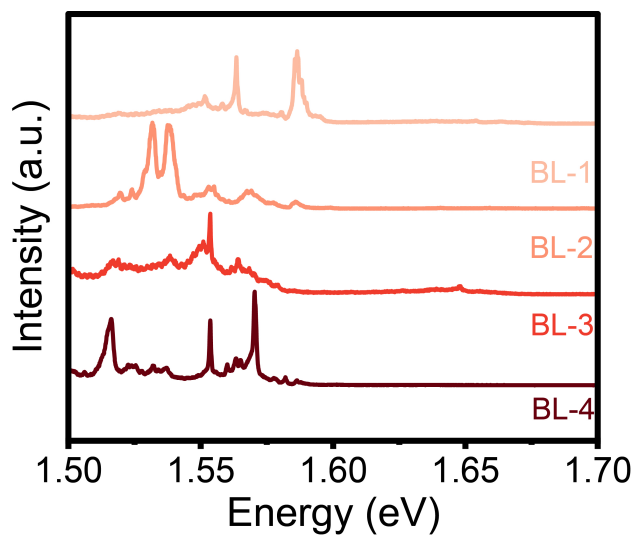


Figure. S11: BL PL spectra of another four spots.

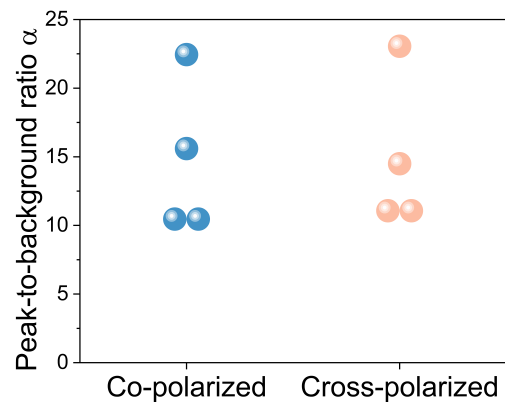


Figure. S12: Peak-to-background ratio α of SPEs in BL using different polarization configurations.

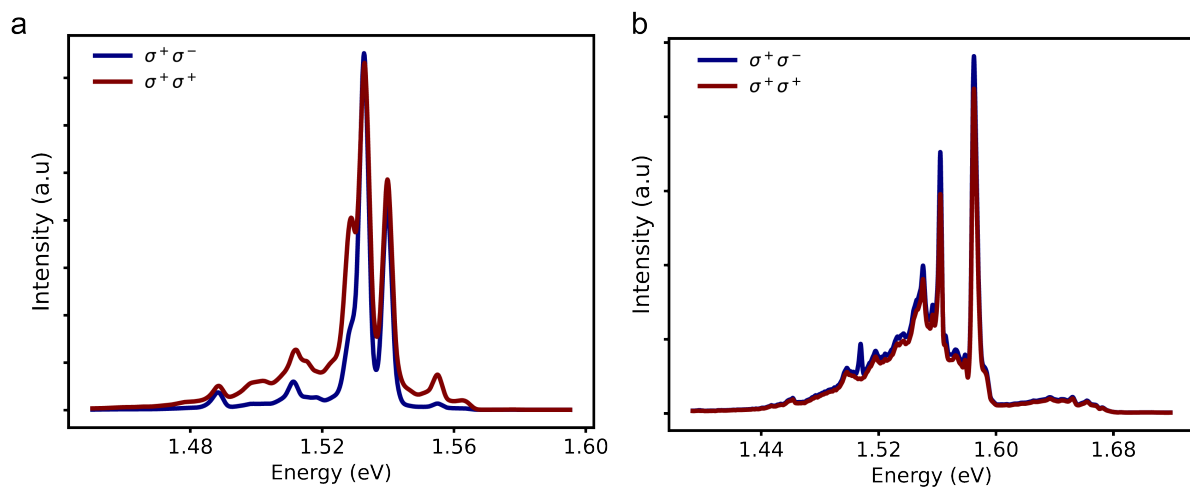


Figure. S13: PL spectra of two extra spots on BL with different optical chirality.

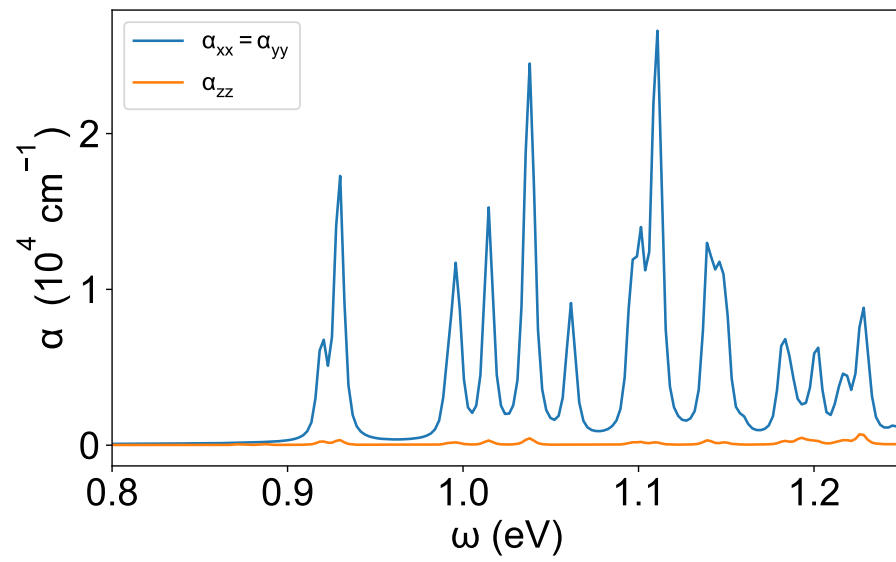


Figure. S14: Frequency-dependent optical absorption coefficient for monolayer WSe₂ with Se vacancy originated from the optical excitation in the defect states.

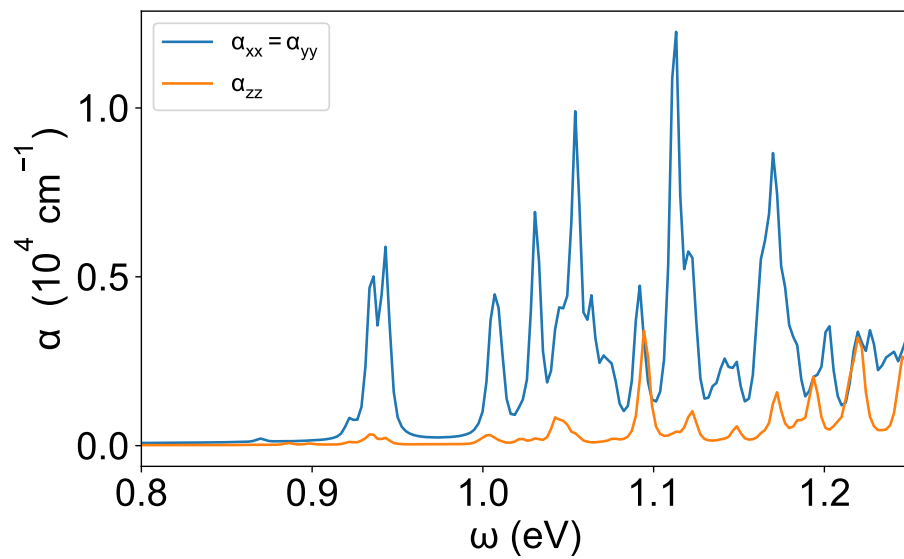


Figure. S15: Frequency-dependent optical absorption coefficient for bilayer WSe₂ with Se vacancy originated from the optical excitation in the defect states.

References

1. Aharonovich, I. *et al.* Diamond-based single-photon emitters **74**, 076501. URL <https://dx.doi.org/10.1088/0034-4885/74/7/076501>.
2. Lohrmann, A., Johnson, B. C., McCallum, J. C. & Castelletto, S. A review on single photon sources in silicon carbide **80**, 034502. URL <https://dx.doi.org/10.1088/1361-6633/aa5171>. Publisher: IOP Publishing.
3. Hadden, J. P. *et al.* Strongly enhanced photon collection from diamond defect centers under microfabricated integrated solid immersion lenses **97**, 241901. URL <https://doi.org/10.1063/1.3519847>.
4. Patel, R. N. *et al.* Efficient photon coupling from a diamond nitrogen vacancy center by integration with silica fiber **5**, e16032–e16032. URL <https://www.nature.com/articles/lsa201632>. Publisher: Nature Publishing Group.
5. Wan, N. H. *et al.* Efficient extraction of light from a nitrogen-vacancy center in a diamond parabolic reflector **18**, 2787–2793. URL <https://doi.org/10.1021/acs.nanolett.7b04684>. Publisher: American Chemical Society.
6. Gupta, S., Wu, W., Huang, S. & Yakobson, B. I. Single-photon emission from two-dimensional materials, to a brighter future **14**, 3274–3284. URL <https://doi.org/10.1021/acs.jpcllett.2c03674>. Number: 13 Publisher: American Chemical Society.
7. Esmann, M., Wein, S. C. & Antón-Solanas, C. Solid-state single-photon sources: Recent advances for novel quantum materials **34**, 2315936. URL <https://doi.org/10.1088/1361-6633/aa5171>.

- onlinelibrary.wiley.com/doi/abs/10.1002/adfm.202315936. eprint:
<https://onlinelibrary.wiley.com/doi/pdf/10.1002/adfm.202315936>.
8. Michaelis de Vasconcellos, S. et al. Single-photon emitters in layered van der waals materials **259**, 2100566. URL <https://onlinelibrary.wiley.com/doi/abs/10.1002/pssb.202100566>. eprint:
<https://onlinelibrary.wiley.com/doi/pdf/10.1002/pssb.202100566>.
9. Zheng, W. et al. Light emission properties of 2d transition metal dichalcogenides: Fundamentals and applications **6**, 1800420. URL <https://onlinelibrary.wiley.com/doi/abs/10.1002/adom.201800420>. eprint:
<https://onlinelibrary.wiley.com/doi/pdf/10.1002/adom.201800420>.
10. Fiori, G. et al. Electronics based on two-dimensional materials **9**, 768–779. URL <https://www.nature.com/articles/nnano.2014.207>. Publisher: Nature Publishing Group.
11. Xia, F., Wang, H., Xiao, D., Dubey, M. & Ramasubramaniam, A. Two-dimensional material nanophotonics **8**, 899–907. URL <https://www.nature.com/articles/nphoton.2014.271>. Publisher: Nature Publishing Group.
12. Hu, Z. et al. Two-dimensional transition metal dichalcogenides: interface and defect engineering **47**, 3100–3128. URL <https://pubs.rsc.org/en/content/articlelanding/2018/cs/c8cs00024g>. Publisher: The Royal Society of Chemistry.

13. Aharonovich, I., Englund, D. & Toth, M. Solid-state single-photon emitters **10**, 631–641. URL <https://www.nature.com/articles/nphoton.2016.186>. Publisher: Nature Publishing Group.
14. Chowdhury, T., Sadler, E. C. & Kempa, T. J. Progress and prospects in transition-metal dichalcogenide research beyond 2d **120**, 12563–12591. URL <https://doi.org/10.1021/acs.chemrev.0c00505>. Publisher: American Chemical Society.
15. Turunen, M. et al. Quantum photonics with layered 2d materials **4**, 219–236. URL <https://www.nature.com/articles/s42254-021-00408-0>. Number: 4 Publisher: Nature Publishing Group.
16. Srivastava, A. et al. Optically active quantum dots in monolayer WSe₂ **10**, 491–496. URL <https://www.nature.com/articles/nnano.2015.60>. Publisher: Nature Publishing Group.
17. Tonndorf, P. et al. Single-photon emission from localized excitons in an atomically thin semiconductor **2**, 347–352. URL <https://opg.optica.org/optica/abstract.cfm?uri=optica-2-4-347>. Publisher: Optica Publishing Group.
18. Koperski, M. et al. Single photon emitters in exfoliated WSe₂ structures **10**, 503–506. URL <https://www.nature.com/articles/nnano.2015.67>. Publisher: Nature Publishing Group.
19. Liang, Q., Zhang, Q., Zhao, X., Liu, M. & Wee, A. T. S. Defect engineering of two-dimensional transition-metal dichalcogenides: Applications, challenges, and opportunities

- 15**, 2165–2181. URL <https://doi.org/10.1021/acsnano.0c09666>. Publisher: American Chemical Society.
20. Wang, Q. H., Kalantar-Zadeh, K., Kis, A., Coleman, J. N. & Strano, M. S. Electronics and optoelectronics of two-dimensional transition metal dichalcogenides **7**, 699–712. URL <https://www.nature.com/articles/nnano.2012.193>. Publisher: Nature Publishing Group.
21. Manzeli, S., Ovchinnikov, D., Pasquier, D., Yazyev, O. V. & Kis, A. 2d transition metal dichalcogenides **2**, 1–15. URL <https://www.nature.com/articles/natrevmats201733>. Publisher: Nature Publishing Group.
22. Mak, K. F. & Shan, J. Photonics and optoelectronics of 2d semiconductor transition metal dichalcogenides **10**, 216–226. URL <https://www.nature.com/articles/nphoton.2015.282>. Publisher: Nature Publishing Group.
23. Gupta, S., Shirodkar, S. N., Kaplan, D., Swaminathan, V. & Yakobson, B. I. Franck condon shift assessment in 2d MoS₂ **30**, 095501. URL <https://dx.doi.org/10.1088/1361-648X/aaa93e>. Publisher: IOP Publishing.
24. Gottscholl, A. *et al.* Initialization and read-out of intrinsic spin defects in a van der waals crystal at room temperature **19**, 540–545. URL <https://www.nature.com/articles/s41563-020-0619-6>. Publisher: Nature Publishing Group.

25. He, Y.-M. *et al.* Single quantum emitters in monolayer semiconductors **10**, 497–502. URL <https://www.nature.com/articles/nnano.2015.75>. Publisher: Nature Publishing Group.
26. Chakraborty, C., Kinnischtzke, L., Goodfellow, K. M., Beams, R. & Vamivakas, A. N. Voltage-controlled quantum light from an atomically thin semiconductor **10**, 507–511. URL <https://www.nature.com/articles/nnano.2015.79>. Publisher: Nature Publishing Group.
27. Rosenberger, M. R. *et al.* Quantum calligraphy: Writing single-photon emitters in a two-dimensional materials platform **13**, 904–912. URL <https://doi.org/10.1021/acsnano.8b08730>. Publisher: American Chemical Society.
28. Klein, J. *et al.* Engineering the luminescence and generation of individual defect emitters in atomically thin MoS₂ **8**, 669–677. URL <https://doi.org/10.1021/acspophotonics.0c01907>. Publisher: American Chemical Society.
29. Branny, A. *et al.* Discrete quantum dot like emitters in monolayer MoSe₂: Spatial mapping, magneto-optics, and charge tuning **108**, 142101. URL <https://doi.org/10.1063/1.4945268>.
30. Zhao, H., Pettes, M. T., Zheng, Y. & Htoon, H. Site-controlled telecom-wavelength single-photon emitters in atomically-thin MoTe₂ **12**, 6753. URL <https://www.nature.com/articles/s41467-021-27033-w>. Publisher: Nature Publishing Group.

31. Kumar, S., Kaczmarczyk, A. & Gerardot, B. D. Strain-induced spatial and spectral isolation of quantum emitters in mono- and bilayer WSe₂ **15**, 7567–7573. URL <https://doi.org/10.1021/acs.nanolett.5b03312>. Publisher: American Chemical Society.
32. Feng, J., Qian, X., Huang, C.-W. & Li, J. Strain-engineered artificial atom as a broad-spectrum solar energy funnel. *Nature Photonics* **6**, 866–872 (2012).
33. Iff, O. *et al.* Strain-tunable single photon sources in WSe₂ monolayers **19**, 6931–6936. URL <https://doi.org/10.1021/acs.nanolett.9b02221>. Publisher: American Chemical Society.
34. Kim, H., Moon, J. S., Noh, G., Lee, J. & Kim, J.-H. Position and frequency control of strain-induced quantum emitters in WSe₂ monolayers **19**, 7534–7539. URL <https://doi.org/10.1021/acs.nanolett.9b03421>. Publisher: American Chemical Society.
35. Parto, K., Azzam, S. I., Banerjee, K. & Moody, G. Defect and strain engineering of monolayer WSe₂ enables site-controlled single-photon emission up to 150 k **12**, 3585. URL <https://www.nature.com/articles/s41467-021-23709-5>. Number: 1 Publisher: Nature Publishing Group.
36. Li, X. *et al.* Proximity-induced chiral quantum light generation in strain-engineered WSe₂/NiPS₃ heterostructures **22**, 1311–1316. URL <https://www.nature.com/articles/s41563-023-01645-7>. Number: 11 Publisher: Nature Publishing Group.

37. Stevens, C. E. et al. Enhancing the purity of deterministically placed quantum emitters in monolayer WSe₂ **16**, 20956–20963. URL <https://doi.org/10.1021/acsnano.2c08553>. Number: 12 Publisher: American Chemical Society.
38. Rosenberger, M. R., Chuang, H.-J., McCreary, K. M., Li, C. H. & Jonker, B. T. Electrical characterization of discrete defects and impact of defect density on photoluminescence in monolayer WS₂ **12**, 1793–1800. URL <https://doi.org/10.1021/acsnano.7b08566>. Publisher: American Chemical Society.
39. Rosenberger, M. R. et al. Nano-“squeegee” for the creation of clean 2d material interfaces **10**, 10379–10387. URL <https://doi.org/10.1021/acsami.8b01224>. Publisher: American Chemical Society.
40. Ye, Y. et al. Single photon emission from deep-level defects in monolayer WSe₂ **95**, 245313. URL <https://link.aps.org/doi/10.1103/PhysRevB.95.245313>. Publisher: American Physical Society.
41. Kern, J. et al. Nanoscale positioning of single-photon emitters in atomically thin WSe₂ **28**, 7101–7105. URL <https://onlinelibrary.wiley.com/doi/abs/10.1002/adma.201600560>. eprint: <https://onlinelibrary.wiley.com/doi/pdf/10.1002/adma.201600560>.
42. Linhart, L. et al. Localized intervalley defect excitons as single-photon emitters in WSe₂ **123**, 146401. URL <https://link.aps.org/doi/10.1103/PhysRevLett.123.146401>. Publisher: American Physical Society.

43. Iff, O. et al. Purcell-enhanced single photon source based on a deterministically placed WSe₂ monolayer quantum dot in a circular bragg grating cavity **21**, 4715–4720. URL <https://doi.org/10.1021/acs.nanolett.1c00978>. Number: 11 Publisher: American Chemical Society.
44. Tang, Y., Mak, K. F. & Shan, J. Long valley lifetime of dark excitons in single-layer WSe₂ **10**, 4047. URL <https://www.nature.com/articles/s41467-019-12129-1>. Number: 1 Publisher: Nature Publishing Group.
45. He, X. et al. Intrinsic limits of defect-state photoluminescence dynamics in functionalized carbon nanotubes **11**, 9125–9132. URL <https://pubs.rsc.org/en/content/articlelanding/2019/nr/c9nr02175b>. Number: 18 Publisher: The Royal Society of Chemistry.
46. Azzam, S. I., Parto, K. & Moody, G. Purcell enhancement and polarization control of single-photon emitters in monolayer WSe₂ using dielectric nanoantennas **12**, 477–484. URL <https://www.degruyter.com/document/doi/10.1515/nanoph-2022-0628/html>. Number: 3 Publisher: De Gruyter.
47. Guo, S. et al. Electrically driven site-controlled single photon source **10**, 2549–2555. URL <https://doi.org/10.1021/acsphotonics.3c00097>. Publisher: American Chemical Society.
48. Serati de Brito, C. et al. Probing the nature of single-photon emitters in a WSe₂ monolayer by magneto-photoluminescence spectroscopy **24**, 13300–13306. URL <https://doi.org/>

- 10.1021/acs.nanolett.4c03686. Publisher: American Chemical Society.
49. Ripin, A. *et al.* Tunable phononic coupling in excitonic quantum emitters **18**, 1020–1026. URL <https://www.nature.com/articles/s41565-023-01410-6>. Number: 9 Publisher: Nature Publishing Group.
50. Mukherjee, A., Chakraborty, C., Qiu, L. & Vamivakas, A. N. Electric field tuning of strain-induced quantum emitters in WSe₂ **10**, 075310. URL <https://doi.org/10.1063/5.0010395>.
51. Chakraborty, C. *et al.* Quantum-confined stark effect of individual defects in a van der waals heterostructure **17**, 2253–2258. URL <https://doi.org/10.1021/acs.nanolett.6b04889>. Publisher: American Chemical Society.
52. Yang, B. *et al.* Effect of distance on photoluminescence quenching and proximity-induced spin-orbit coupling in graphene/WSe₂ heterostructures **18**, 3580–3585. URL <https://doi.org/10.1021/acs.nanolett.8b00691>. Publisher: American Chemical Society.
53. Schwarz, S. *et al.* Electrically pumped single-defect light emitters in WSe₂ **3**, 025038. URL <https://iopscience.iop.org/article/10.1088/2053-1583/3/2/025038>.
54. Chen, X. *et al.* Entanglement of single-photons and chiral phonons in atomically thin WSe₂ **15**, 221–227. URL <https://www.nature.com/articles/s41567-018-0366-7>. Publisher: Nature Publishing Group.

55. Jones, A. M. et al. Optical generation of excitonic valley coherence in monolayer WSe₂ **8**, 634–638. URL <https://www.nature.com/articles/nnano.2013.151>. Number: 9 Publisher: Nature Publishing Group.
56. He, M. et al. Valley phonons and exciton complexes in a monolayer semiconductor **11**, 618. URL <https://www.nature.com/articles/s41467-020-14472-0>. Number: 1 Publisher: Nature Publishing Group.
57. Huang, Z. et al. Spatially indirect intervalley excitons in bilayer WSe₂ **105**, L041409. URL <https://link.aps.org/doi/10.1103/PhysRevB.105.L041409>. Publisher: American Physical Society.
58. Helversen, M. v. et al. Temperature dependent temporal coherence of metallic-nanoparticle-induced single-photon emitters in a WSe₂ monolayer **10**, 045034. URL <https://dx.doi.org/10.1088/2053-1583/acfb20>. Number: 4 Publisher: IOP Publishing.
59. Gao, T., von Helversen, M., Antón-Solanas, C., Schneider, C. & Heindel, T. Atomically-thin single-photon sources for quantum communication **7**, 1–9. URL <https://www.nature.com/articles/s41699-023-00366-4>. Publisher: Nature Publishing Group.
60. Grünwald, P. Effective second-order correlation function and single-photon detection **21**, 093003. URL <https://dx.doi.org/10.1088/1367-2630/ab3ae0>. Publisher: IOP Publishing.

61. Luo, Y., Liu, N., Li, X., Hone, J. C. & Strauf, S. Single photon emission in WSe₂ up to 160 K by quantum yield control **6**, 035017. URL <https://dx.doi.org/10.1088/2053-1583/ab15fe>. Number: 3 Publisher: IOP Publishing.
62. Moon, H. et al. Strain-correlated localized exciton energy in atomically thin semiconductors **7**, 1135–1140. URL <https://doi.org/10.1021/acsphotonics.0c00626>. Number: 5 Publisher: American Chemical Society.
63. Utama, M. I. B. et al. Chemomechanical modification of quantum emission in monolayer WSe₂ **14**, 2193. URL <https://www.nature.com/articles/s41467-023-37892-0>. Publisher: Nature Publishing Group.
64. Palacios-Berraquero, C. et al. Atomically thin quantum light-emitting diodes **7**, 12978. URL <https://www.nature.com/articles/ncomms12978>. Number: 1 Publisher: Nature Publishing Group.
65. Palacios-Berraquero, C. et al. Large-scale quantum-emitter arrays in atomically thin semiconductors **8**, 15093. URL <https://www.nature.com/articles/ncomms15093>. Publisher: Nature Publishing Group.
66. Komsa, H.-P. et al. Two-dimensional transition metal dichalcogenides under electron irradiation: Defect production and doping **109**, 035503. URL <https://link.aps.org/doi/10.1103/PhysRevLett.109.035503>. Publisher: American Physical Society.

67. Chuang, H.-J. *et al.* Enhancing single photon emission purity via design of van der waals heterostructures **24**, 5529–5535. URL <https://doi.org/10.1021/acs.nanolett.4c00683>. Publisher: American Chemical Society.
68. Xu, D. D. *et al.* Conversion of classical light emission from a nanoparticle-strained WSe₂ monolayer into quantum light emission via electron beam irradiation **35**, 2208066. URL <https://onlinelibrary.wiley.com/doi/abs/10.1002/adma.202208066>. Number: 5 eprint: <https://onlinelibrary.wiley.com/doi/pdf/10.1002/adma.202208066>.
69. Sharma, P. *et al.* Nonvolatile ferroelectric domain wall memory **3**, e1700512. URL <https://www.science.org/doi/10.1126/sciadv.1700512>. Publisher: American Association for the Advancement of Science.
70. Barbone, M. *et al.* Charge-tuneable biexciton complexes in monolayer WSe₂ **9**, 3721. URL <https://www.nature.com/articles/s41467-018-05632-4>. Publisher: Nature Publishing Group.
71. Jin, C. *et al.* Interlayer electron–phonon coupling in WSe₂/hBN heterostructures **13**, 127–131. URL <https://www.nature.com/articles/nphys3928>. Publisher: Nature Publishing Group.
72. Zhao, H. *et al.* High-purity generation and switching of twisted single photons **131**, 183801. URL <https://link.aps.org/doi/10.1103/PhysRevLett.131.183801>. Publisher: American Physical Society.

73. Branny, A., Kumar, S., Proux, R. & Gerardot, B. D. Deterministic strain-induced arrays of quantum emitters in a two-dimensional semiconductor **8**, 15053. URL <https://www.nature.com/articles/ncomms15053>. Publisher: Nature Publishing Group.
74. Liu, S. et al. Two-step flux synthesis of ultrapure transition-metal dichalcogenides **17**, 16587–16596. URL <https://doi.org/10.1021/acsnano.3c02511>. Publisher: American Chemical Society.
75. Schädler, K. G. et al. Electrical control of lifetime-limited quantum emitters using 2d materials **19**, 3789–3795. URL <https://doi.org/10.1021/acs.nanolett.9b00916>. Publisher: American Chemical Society.
76. Fox, A. M. Quantum Optics: An Introduction (OUP Oxford). Google-Books-ID: 2YES-DAAAQBAJ.
77. Robert, C. et al. Exciton radiative lifetime in transition metal dichalcogenide monolayers **93**, 205423. URL <https://link.aps.org/doi/10.1103/PhysRevB.93.205423>. Publisher: American Physical Society.
78. Abramov, A. N. et al. Photoluminescence imaging of single photon emitters within nanoscale strain profiles in monolayer WSe₂ **14**, 5737. URL <https://www.nature.com/articles/s41467-023-41292-9>. Number: 1 Publisher: Nature Publishing Group.

79. So, J.-P. *et al.* Polarization control of deterministic single-photon emitters in monolayer WSe₂ **21**, 1546–1554. URL <https://doi.org/10.1021/acs.nanolett.1c00078>. Number: 3 Publisher: American Chemical Society.
80. Qian, Q. *et al.* Defect creation in WSe₂ with a microsecond photoluminescence lifetime by focused ion beam irradiation **12**, 2047–2056. URL <https://pubs.rsc.org/en/content/articlelanding/2020/nr/c9nr08390a>. Publisher: Royal Society of Chemistry.
81. Palummo, M., Bernardi, M. & Grossman, J. C. Exciton radiative lifetimes in two-dimensional transition metal dichalcogenides **15**, 2794–2800. URL <https://doi.org/10.1021/n1503799t>. Publisher: American Chemical Society.
82. Xiao, D., Liu, G.-B., Feng, W., Xu, X. & Yao, W. Coupled spin and valley physics in monolayers of MoS_2 and other group-VI dichalcogenides **108**, 196802. URL <https://link.aps.org/doi/10.1103/PhysRevLett.108.196802>. Publisher: American Physical Society.
83. Cao, T. *et al.* Valley-selective circular dichroism of monolayer molybdenum disulphide **3**, 887. URL <https://www.nature.com/articles/ncomms1882>. Publisher: Nature Publishing Group.
84. Mak, K. F., He, K., Shan, J. & Heinz, T. F. Control of valley polarization in monolayer MoS₂ by optical helicity **7**, 494–498. URL <https://www.nature.com/articles/nnano.2012.96>. Publisher: Nature Publishing Group.

85. Lindlau, J. et al. The role of momentum-dark excitons in the elementary optical response of bilayer WSe₂ **9**, 2586. URL <https://www.nature.com/articles/s41467-018-04877-3>. Publisher: Nature Publishing Group.
86. Wang, Y. et al. Efficient quantum memory for single-photon polarization qubits **13**, 346–351. URL <https://www.nature.com/articles/s41566-019-0368-8>. Publisher: Nature Publishing Group.
87. Specht, H. P. et al. A single-atom quantum memory **473**, 190–193. URL <https://www.nature.com/articles/nature09997>. Publisher: Nature Publishing Group.
88. Komsa, H.-P. et al. Two-dimensional transition metal dichalcogenides under electron irradiation: Defect production and doping **109**, 035503. URL <https://link.aps.org/doi/10.1103/PhysRevLett.109.035503>. Publisher: American Physical Society.
89. Hohenberg, P. & Kohn, W. Inhomogeneous Electron Gas. Physical Review **136**, B864–B871 (1964). URL <https://link.aps.org/doi/10.1103/PhysRev.136.B864>.
90. Kohn, W. & Sham, L. J. Self-Consistent Equations Including Exchange and Correlation Effects. Physical Review **140**, A1133–A1138 (1965). URL <https://link.aps.org/doi/10.1103/PhysRev.140.A1133>.
91. Kresse, G. & Furthmüller, J. Efficient iterative schemes for ab initio total-energy calculations using a plane-wave basis set. Physical Review B **54**, 11169–11186 (1996). URL <https://link.aps.org/doi/10.1103/PhysRevB.54.11169>.

92. Kresse, G. & Furthmüller, J. Efficiency of ab-initio total energy calculations for metals and semiconductors using a plane-wave basis set. *Computational Materials Science* **6**, 15–50 (1996). URL <https://www.sciencedirect.com/science/article/pii/0927025696000080>.
93. Blöchl, P. E. Projector augmented-wave method. *Physical Review B* **50**, 17953–17979 (1994).
94. Perdew, J. P., Burke, K. & Ernzerhof, M. Generalized gradient approximation made simple. *Physical Review Letters* **77**, 3865–3868 (1996).
95. Grimme, S., Antony, J., Ehrlich, S. & Krieg, H. A consistent and accurate ab initio parametrization of density functional dispersion correction (DFT-D) for the 94 elements H-Pu. *Journal of Chemical Physics* **132** (2010).
96. Monkhorst, H. J. & Pack, J. D. Special points for Brillouin-zone integrations. *Physical Review B* **13**, 5188 (1976).
97. Popescu, V. & Zunger, A. Extracting E versus k effective band structure from supercell calculations on alloys and impurities. *Physical Review B* **85**, 085201 (2012). URL <https://link.aps.org/doi/10.1103/PhysRevB.85.085201>.
98. Zheng, Q. VASP Band Unfolding. <https://github.com/QijingZheng/VaspBandUnfolding>.